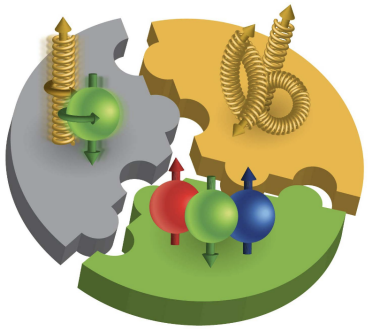

Brookhaven National Laboratory

Hadron Polarimetry at the Electron-Ion Collider

Challenges and Solutions

Frank Rathmann
for the EIC and CAD Polarimetry Group

Brookhaven National Laboratory

CAD MAC Meeting, December 17, 2025

Contents

Introduction

Hadron polarimetry requirements for the EIC I

Deliverables

- The EIC will use polarized **protons** ($\vec{p}$) and **helions** ($\vec{h} = {}^{3}\overrightarrow{\mathrm{He}}$), later on deuterons ($\vec{d}$), and heavier nuclei like lithium ${}^{6,7}\overrightarrow{\mathrm{Li}}$) may be needed.
- **The EIC promises to provide proton beam polarizations of $P \geq 0.7$ with a relative uncertainty of $\Delta P/P \leq 1\%$.**
- Polarization calibration needed for each ion species as presently done:
  - elastic scattering of identical particles $\Rightarrow$ beam polarization inferred from known target polarization.
- **Absolute proton beam polarization calibration relies on measured nuclear polarization of atomic jet using Breit-Rabi polarimeter.**

Hadron polarimetry requirements for the EIC II

Instruments

- Hadron polarimeter (absolute) in **IP4**
- pC polarimeter (relative) in **IP4** and **IP6** (between spin rotators)

Polarimeters shall determine:

- Bunch polarization profile in x, y, z
- Polarization lifetime
  - For EIC physics, projection of $\vec{P}$ on stable spin axis required, no in-plane polarization.
- Polarization vector $\vec{P}$ per bunch

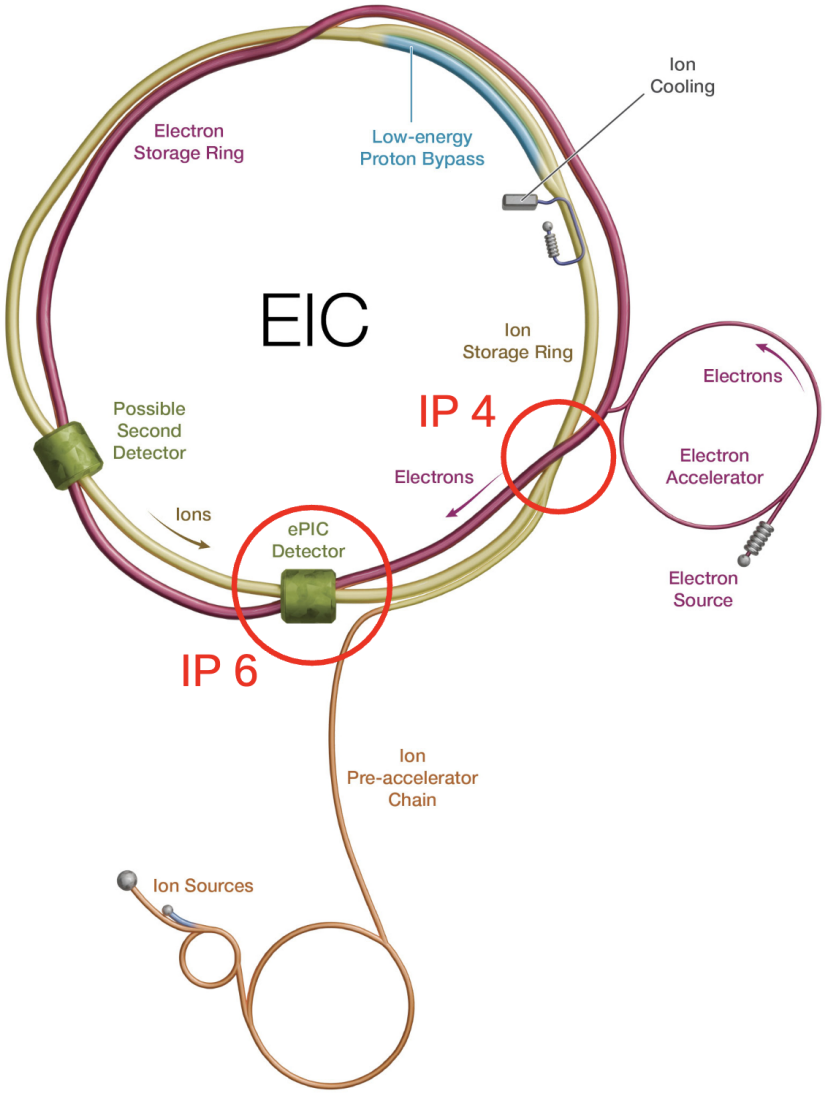

Instruments

Instruments for absolute and relative polarimetry

Two devices

- **HJET polarimeter**

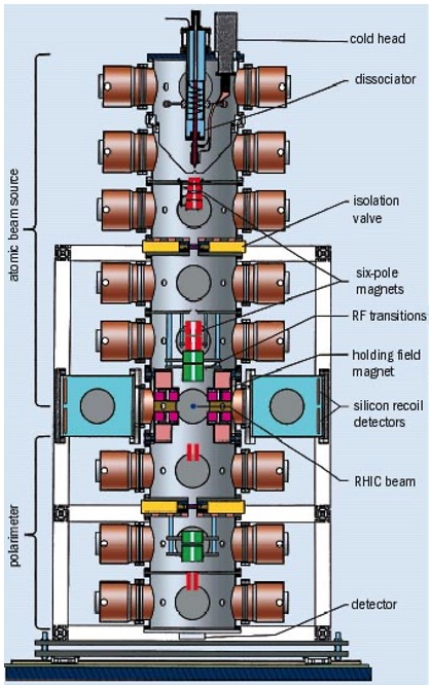

  - **absolute, slow**

$$\frac{\Delta P}{P} \approx 3\% \text{ per } 4 \text{ hour} \quad (1)$$

- **pC polarimeters**

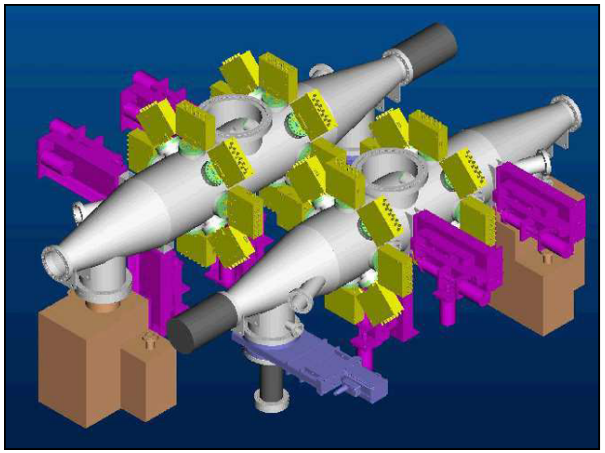

  - **fast, relative**
  - transverse profiles of polarization

$$\frac{\Delta P}{P} < 1\% \text{ per scan} \quad (2)$$

(See slides 48*ff* for further details)

Absolute beam polarization

Absolute polarization from polarized hydrogen jet I

Breit-Rabi polarimeter

- Capable to determine absolute polarization Q of atomic beam, i.e., electron and proton polarization of hydrogen atoms, with accuracy $\Delta Q/Q \lesssim 1\%$.
  - No solid estimates available that fully encapsulate the BRP measurement systematics at the HJET on the $\approx 1\%$ level [1]

Beam polarization calibration

1. Proton beam passes through target of polarized H atoms of known polarization Q

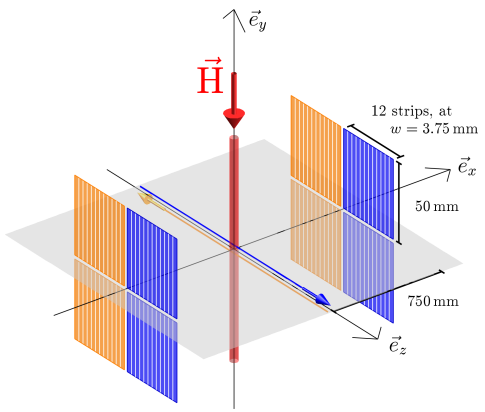

Absolute polarization from polarized hydrogen jet II

Beam polarization calibration

2. Measure number of scattered particles in left (L) and right (R) detectors (at $\phi = 0$ and $\phi = \pi$, respectively).
3. Sign of Q is periodically reversed to compensate for asymmetries caused by differences in detector geometry or efficiency in L and R directions.
4. This determines target asymmetry

$$\epsilon_{\text{target}} = \frac{\text{L} - \text{R}}{\text{L} + \text{R}} = A_y \cdot Q \,. \tag{3}$$

5. Measurement of corresponding asymmetry with beam particles determines ϵ_{beam}. In elastic pp scattering, and more general in the elastic scattering of *identical* particles, A_y same regardless of which proton is polarized.
6. Absolute beam polarization given by

$$\boxed{P = \frac{\epsilon_{\text{beam}}}{\epsilon_{\text{target}}} \cdot Q} \tag{4}$$

Beam-induced target depolarization

Beam-induced target depolarization at RHIC and EIC

- At EIC, the bunch repetition frequency is much larger than at RHIC → **investigate beam-induced depolarization of target atoms** (full analysis discussed in [1]).

RHIC situation:

- Time period between two adjacent bunches: $\tau_\mathrm{b} = \frac{\tau_\mathrm{rev}}{N_b} = 106.598\,\mathrm{ns}$
- Number of stored bunches $N_b = 120$
- Bunch frequency $f_\mathrm{b} = \frac{1}{\tau_\mathrm{b}} = 9.381\,\mathrm{MHz}$
- Large number of harmonics contribute to induced magnetic high-frequency field close to RHIC beam, as bunches are short ($\sigma_t \approx 1.8\,\mathrm{ns}$)

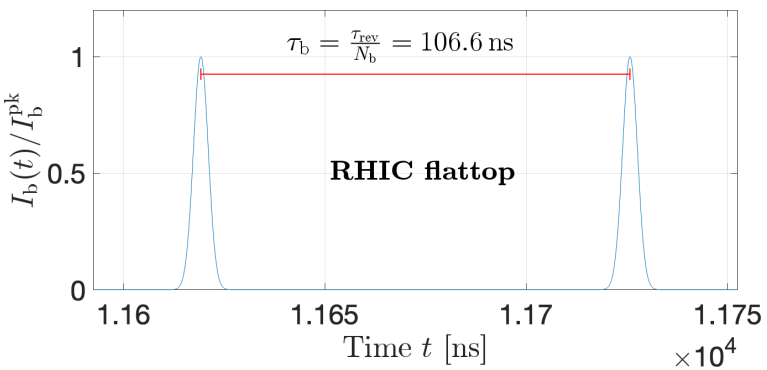

Elimination of beam-induced H target depolarization at EIC

Solutions

1. At RHIC, B-field was moved to $\approx 120\,\mathrm{mT}$ and $\frac{f_{ij}}{f_{\mathrm{b}}^{\mathrm{RHIC}}} \geq 350$ ignored (slide 57)
2. **For EIC: $\Rightarrow$ push harmonics to ≥ 100 $\Rightarrow$ holding field $\geq 400\,\mathrm{mT}$**

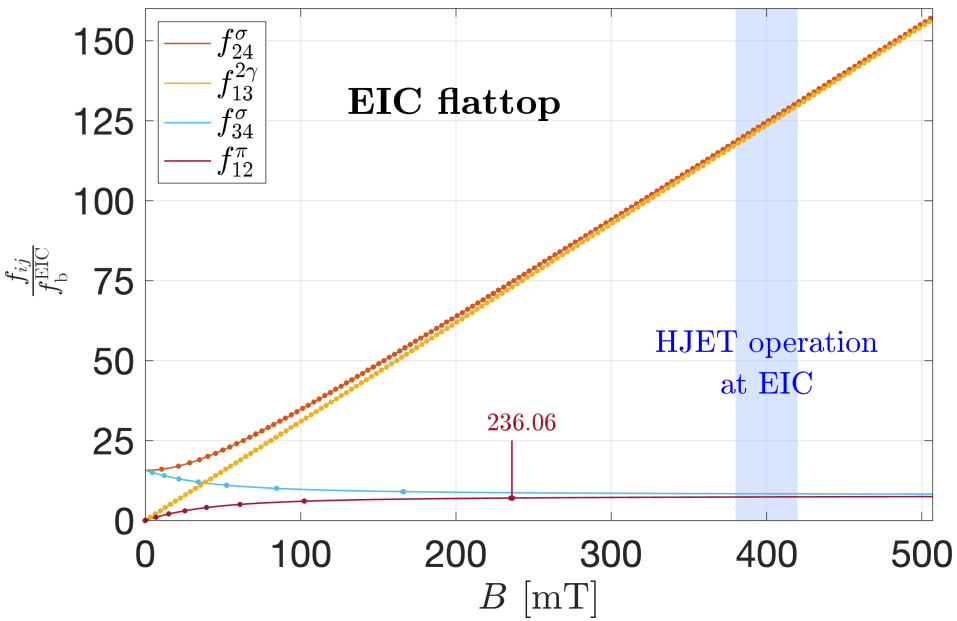

Resonances f_{34}^{σ} and f_{12}^{π}

- Become harmless (die out) above $\approx 236.06\,\mathrm{mT}$

- For further details, see spare slides 55*ff*

Magnetic target guide field

Concept for magnetic guide field for HJET at EIC

But first ...

Spin-dependent *pp* elastic cross section (spin 1/2 + spin 1/2)

With polarized beam $\vec{P}$ and polarized target $\vec{Q}$, all components of $\vec{P}$ can be determined from spin-dependent cross section, as shown in Table below [4, 5]:

$$\begin{aligned}\sigma/\sigma_0 = 1 &+ A_y \left[(P_y + Q_y)\cos\phi - (P_x + Q_x)\sin\phi\right] \\ &+ A_{xx}\left[P_x Q_x \cos^2\phi + P_y Q_y \sin^2\phi + (P_x Q_y + P_y Q_x)\sin\phi\cos\phi\right] \\ &+ A_{yy}\left[P_x Q_x \sin^2\phi + P_y Q_y \cos^2\phi - (P_x Q_y + P_y Q_x)\sin\phi\cos\phi\right] \\ &+ A_{xz}\left[(P_x Q_z + P_z Q_x)\cos\phi + (P_y Q_z + P_z Q_y)\sin\phi\right] + A_{zz} P_z Q_z\end{aligned}$$

- Full angular distributions of all A_{ik}'s were determined.
- Single input: $A_y = 0.2122 \pm 0.0017$ at $\theta_{\text{lab}} = 8.64^\circ \pm 0.07^\circ$ [6], known from $A_y = 1$ point in $p + {}^{12}\text{C}$ elastic scattering [7].

Most importantly in context

- determination of beam $\vec{P} = (P_x, P_y, P_z)$ and target $\vec{Q} = (Q_x, Q_y, Q_z)$, as well as non-flipping components possible (slide 66)

Spin-dependent pp elastic cross section

The above is relevant for two reasons

1. The spin-dependence of $\vec{p}\vec{p}$ elastic scattering allows to reconstruct angular distributions of all (in that case five) polarization observables.
2. With suitable magnetic guide field, target polarization $\vec{Q}$ can be oriented along any direction, for instance along x, so that $\vec{Q} = Q \cdot \vec{e}_x = \vec{Q}_x$
   - Absolute value of target polarization Q determined by BRP

Two things needed to port HJET from RHIC to EIC with $\frac{\Delta P}{P} \leq 1\%$

1. Substantially stronger holding field of $|\vec{B}| \approx 400\,\mathrm{mT}$ than at RHIC
2. Enable detector to see azimuthal asymmetries $\propto \sin\phi$ and $\propto \sin 2\phi$ (slide 67)
   - foresee proper detector symmetry to provide $\vec{d}\vec{d}$ beam absolute polarimetry, i.e., beyond $\propto \sin 3\phi$.

Holding field system for $|\vec{B}| \approx 0.3\,\mathrm{T}$ with $\vec{B} \parallel \vec{e}_{x,y,z}$

Work in part together with Helmut Soltner (FZJ, Germany)

Motivation:

- Reconcile strong magnetic holding field with open detector geometry to determine, e.g., all spin components of beam polarization $\vec{P} = (P_x, P_y, P_z)$
- Exploit magnetic moments $\vec{m}$ of homogeneously magnetized spheres [8–10]
- Invert $\vec{m}$ in vacuum to reverse $\vec{B}(O)$
- Reorient $\vec{m}$'s to generate $\vec{B}(O) \parallel \vec{e}_{x,y,z}$

Consider two sets of frames

- Beam meets atoms at (O)
  - Set 1: $100\,\mathrm{mm}_x \times 100\,\mathrm{mm}_y \times 40\,\mathrm{mm}_z$
  - Set 2: $100\,\mathrm{mm}_x \times 100\,\mathrm{mm}_y \times 110\,\mathrm{mm}_z$
  - 8 magnetized spheres in corners of frames:
  - NeFeB magnets provide remanence of $B_r = 1.49 - 1.55\,\mathrm{T}$ (type N58)
  - Radius $r = 30\,\mathrm{mm}$

Holding field system

Together with Helmut Soltner (FZJ, Germany)

- Flux density vector as fct of $\vec{m}$ in space

$$\vec{B}(\vec{r}) = \frac{\mu_0}{4\pi}\left[\frac{3\left(\vec{m}\cdot\hat{R}\right)\hat{R}-\vec{m}}{|R|^3}\right] \quad (5)$$

$$\vec{R} = \vec{r} - \vec{r}_0, \hat{R} = \frac{\vec{R}}{|R|}$$

- Optimize orientation of $\vec{m}$'s to maximize $\vec{B}(O)$ along $\vec{e}_x$, $\vec{e}_y$, or $\vec{e}_z$
  - maximize dot product $\vec{m}\cdot\hat{R}$, set $m_y = 0$ to obtain, e.g., max. B_y

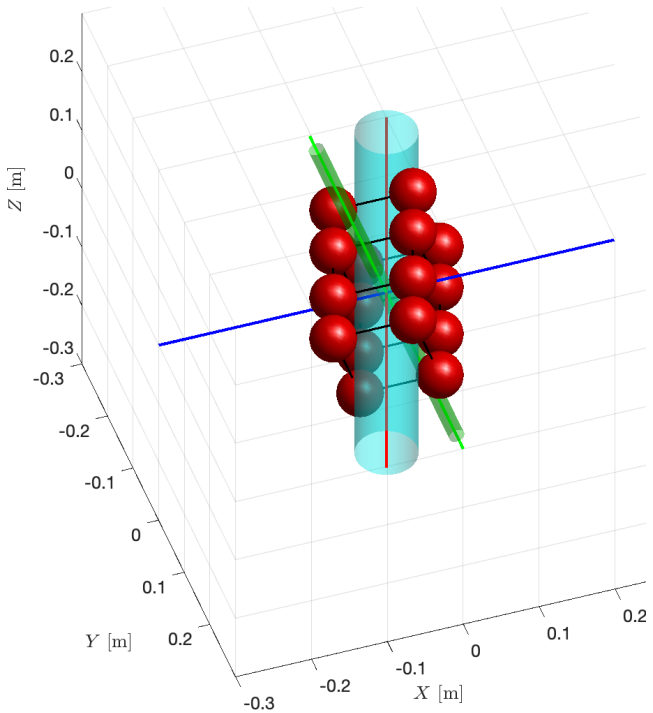

e.g., 16 spherical magnetic dipoles

- atomic beam $\parallel \vec{e}_y$ and ion beam $\parallel \vec{e}_z$
- For technical realization and further details, see slides 68*ff*

pC polarimetry

Will carbon fiber targets survive at EIC?

Estimated target heating using code by Peter Thieberger (BNL)

- Increased beam sizes at EIC $\Rightarrow$ thin fibers remain applicable for EIC.
- RF heating of holders more severe at EIC due to shorter bunches.
  $\Rightarrow$ **optimize RF design of target holders**

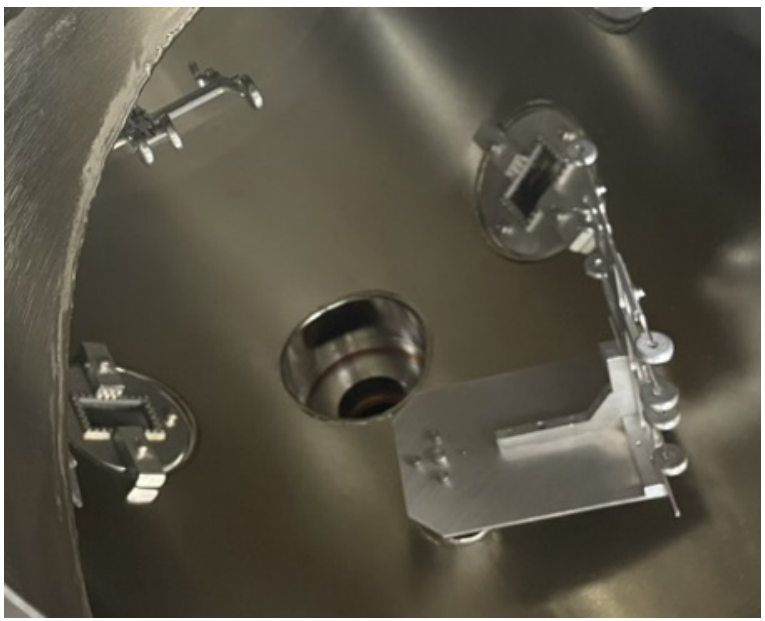

- Direct temperature measurements of targets is in progress (see slide 79)

Carbon target temperatures from Thieberger's model

Typical conditions, assuming round EIC beam

- **RHIC:** 250 GeV, 111 bunches, 16×10^{10} protons/bunch, $\sigma_r^{95} = 0.68$ mm.
- **EIC:** 275 GeV, 1160 bunches, 6.9×10^{10} protons/bunch, $\sigma_r^{95} = 1.2$ mm.

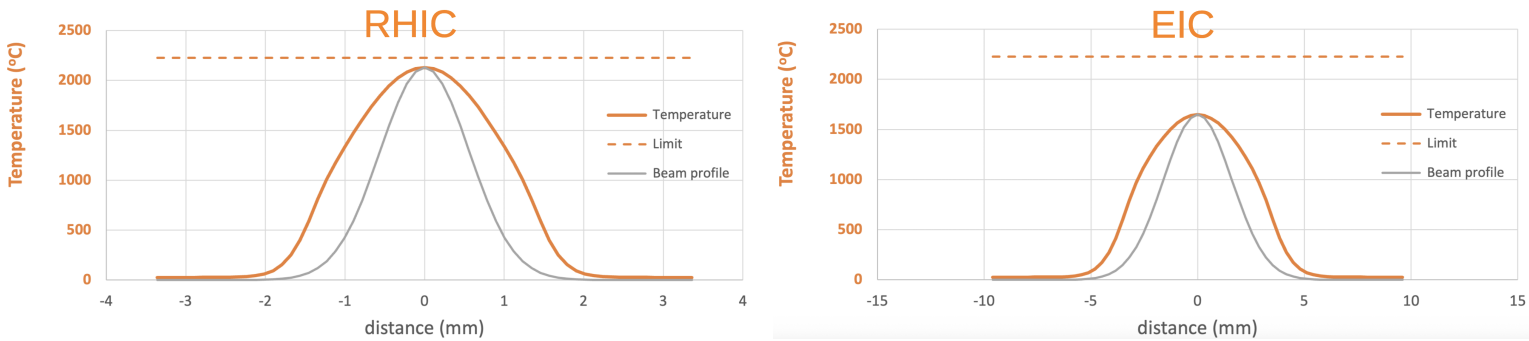

Thermal modeling of carbon ribbon targets

- Despite higher EIC beam energy and total current, the larger transverse beam size lowers power density and keeps the peak temperature below the carbon sublimation temperature $T_{\text{sub}} = 3915$ K [12].
- For pC ribbons in UHV, conservative continuous operation is typically below 3200 K to 3500 K to limit mass loss (see slide 80), but Thieberger's code [13] uses $T_{\text{melt}} = 2227$ K while carbon sublimes.

Further details, see slides *77ff*

Wakefield simulations (pC target system)

Medani Sangroula (BNL)

- Wakefields from pC chamber and target holder near beam critical at EIC due to short bunches and rich harmonic content.
- Objective: minimize longitudinal impedance $Z_{\parallel}(f)$ and local power.
- Design lever: dielectric holder (e.g. Al_2O_3) with thin conductive coating for charge control; metallic features are RF-shielded.

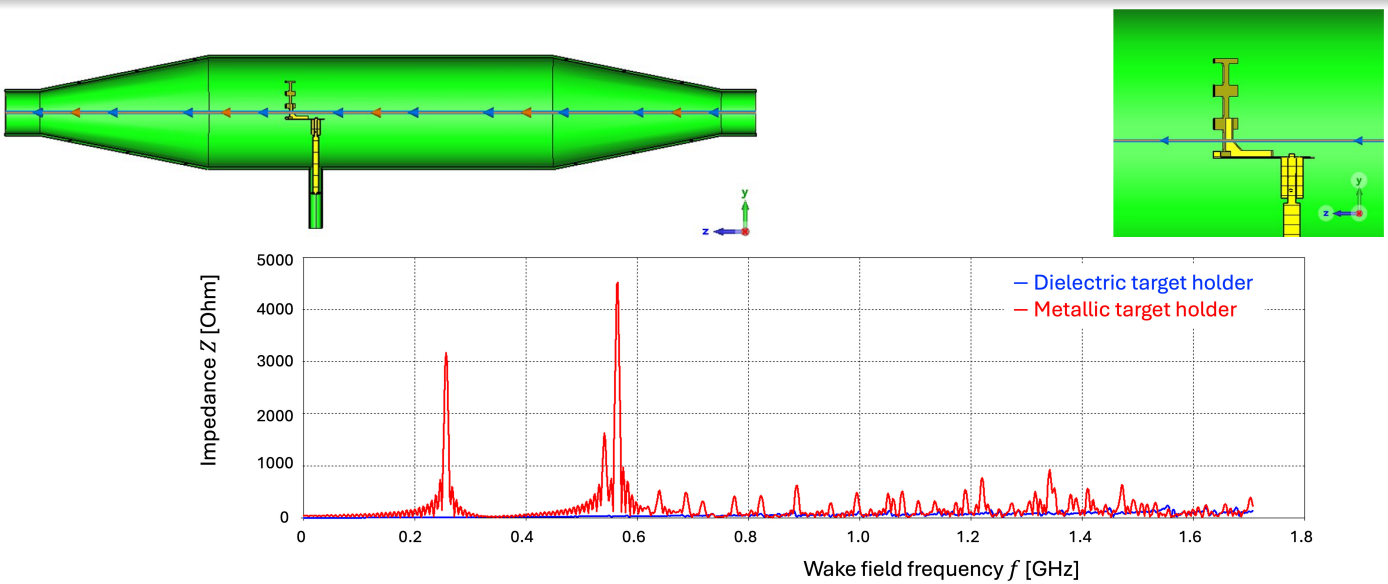

Wake impedance $Z(f)$: metallic (Al holder in SS chamber) vs. dielectric (Al_2O_3) holder

Findings

- Dielectric holders (e.g. Al_2O_3) reduce wake impedance vs. metallic designs.
- Thin conductive coating (charge) $\Rightarrow$ negligible impact on $Z(\omega)$.

Wakefield simulations (holder positioning)

- Move the dielectric target holder away from beam (0 mm → 38.1 mm → 76.2 mm).
- Goal: reduce wake potential $W(s)$ and local RF power deposition near the intercept.

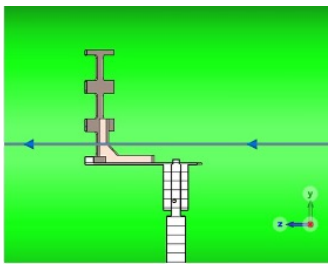

Target holder at 0 mm.

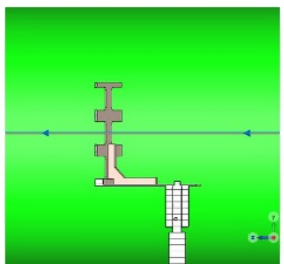

Target holder at 38.1 mm.

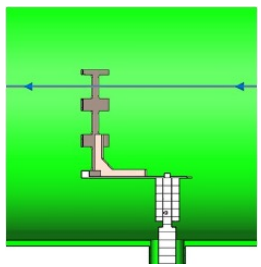

Target holder at 76.2 mm.

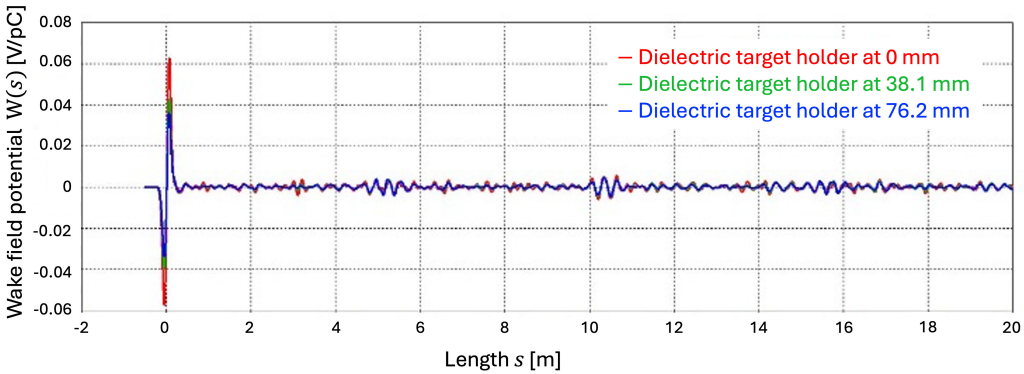

Wake potential $W(s)$: systematic reduction with increasing displacement toward chamber wall.

Findings

- Displacing dielectric holder away from beam reduces $W(s)$ across band of interest.
- Recommendation: RF shielding of nearby ports/feedthroughs.
- One-target-in-chamber minimizes impedance and simplifies operation.

Other polarized beam species

Polarized ^{3}He target

Option 1: Polarized ^{3}He Atomic Beam Source

Original MIT development for nEDM exp't at Oakridge

- Prajwal T. MohanMurthy, J. Kelsey, J. Dodge, R. Redwine, R. Milner, P. Binns, B. O'Rourke
- nEDM experiment at ORNL discontinued

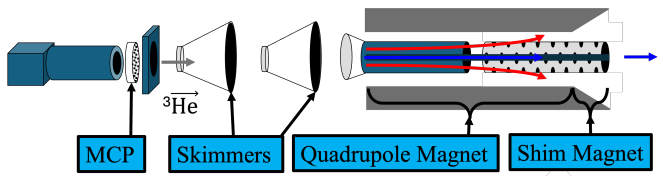

$^3\vec{\text{He}}$: quadrupole magnet selects spins
- 1.3 K ≈ 86 μeV
- $\Delta E = \mu_m \approx 67$ neV/T
- initial angle very important

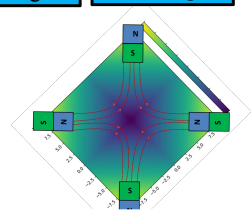

Atomic flux

- With $1 \times 10^{14}\,\text{s}^{-1} \Rightarrow$ bare-jet $d_t \approx 1.3 \times 10^{10}\,\text{cm}^{-2}$
  - Assumptions: $D = 1.0\,\text{cm}$ (uniform), $L = 1\,\text{cm}$, $T = 1.3\,\text{K}$.
- With storage cell (molecular flow, $T = 77\,\text{K}$): $d_t \approx 1.0 \times 10^{12}\,\text{cm}^{-2}$
  - Geometry: $\ell_{\text{inj}} = 10\,\text{cm}$, $\ell_{\text{up}} = \ell_{\text{down}} = 30\,\text{cm}$, $\ell_t = 60\,\text{cm}$ (see slide 90).
- **Well-suited for absolute $^3\vec{\text{He}}^{++}$ beam polarimetry at EIC.**

Polarized ^{3}He target

Option 2: Laser-driven target

Key features and performance [14]

- Laser-driven metastability-exchange optical pumping (MEOP):
  - weak RF discharge populates metastable 2^3S_1 state
  - circularly polarized 1083 nm light transfers angular momentum to ^{3}He gas.

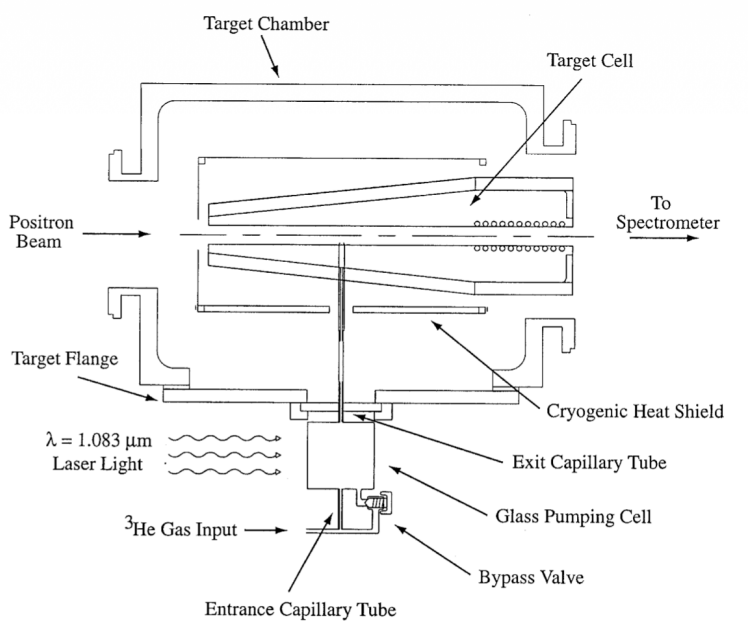

$2.8M DOE grant submitted by Bates (PMM) to develop MEOP polarized target

- Operated in HERMES experiment at HERA/DESY (1997–2000)
- cryogenic aluminum target cell cooled to $\approx 25\,\text{K}$
- nuclear polarizations up to 54 %
- areal target thickness $d_t \approx 10^{15}$ nucleons/cm^2

Absolute polarimetry of $\vec{d}$ beams

Polarized atomic deuterium jet

- Atomic beam sources efficiently produce beams of deuterium atoms
- Use of dual-function RF transition units for $\vec{\text{H}}$ and $\vec{\text{D}}$ atoms ideal [15].
- With vector and tensor polarization accurately determined by BRP, absolute beam polarimetry based on $\vec{d}\vec{d}$ elastic scattering becomes possible
  - + B_x, B_y, B_z options will allow reconstruction of beam polarization $\vec{P} = (P_x, P_y, P_z)$ vector, incl. tensor components (see slide 15).
- For measurement strategy, asymmetries, and p_z, p_{zz} extraction, see slide 87.

EIC hadron polarimetry at IP4

Carbon, polarized H, and ^{3}He gas targets at a single IP

- **Co–location** minimizes spin transport between devices
- **Common services:** unified slow controls and DAQ.
- **Functional roles:** carbon ribbon(s) for fast relative P scans; polarized H (HJET) and ^{3}He for absolute P calibration.

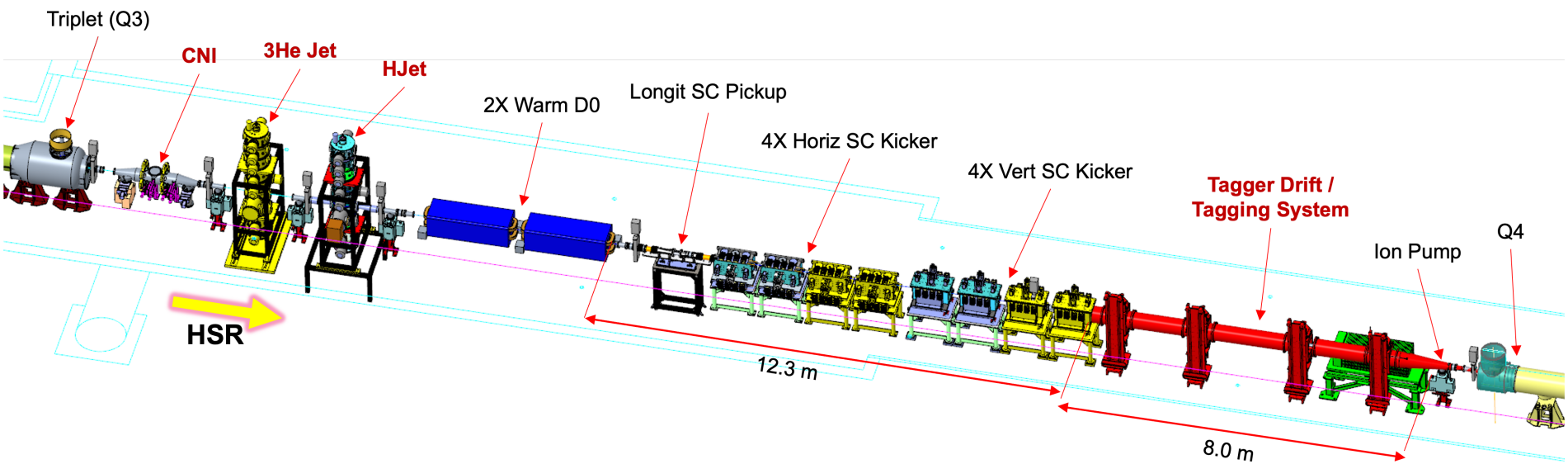

Storage cell-based polarimetry in the AGS

Storage cell-based polarimetry in the AGS

Based on PAX developments for COSY [16]

Concept

- Use an openable storage cell in the AGS to provide a high areal target density d_t for CNI *pp* elastic polarimetry and related reactions.
- Initially, fill the cell with unpolarized gas, e.g., H_2, to generate the required target densities for a variety of polarimetry reactions.
- At a later stage, a polarized H (or D) atomic beam can be used to feed the storage cell and provide a polarized internal target.

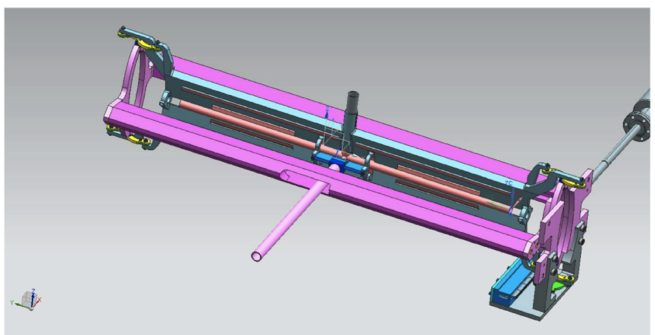

PAX openable storage cell [16], in closed position. Polarized atoms are injected through the upper tube (blue). Target gas exits towards BRP through side tube (pink).

Storage cell-based polarimetry in the AGS

Features

- High and tunable areal target density d_t with a wide choice of gas species (H_2, D_2, CH_4, CO_2, N_2, O_2, ...) for optimizing polarimetry.
- Very large solid-angle acceptance using the PAX detector system.
- **Goal:**
  - enable continuous polarization measurements during the upramp from about 3 GeV to 23.5 GeV in AGS.
  - With a storage-cell target driven by injected unpolarized gas from a feeding system, target density can be suitably varied during the upramp.
- At present, polarization is measured at discrete energies using sweeping carbon-fiber targets; a **storage-cell target would provide continuous polarimetry along the ramp**.

Existing hardware: ready for reuse and integration

- All equipment shown in following: target chamber, thin-foil openable cell, test chambers, detector system, etc., available (stored at Ferrara University)

Storage cell-based polarimetry in the AGS

Based on PAX developments for COSY [16]

Detector system

- RHIC: 2 detectors per beam at $\phi = 0°, 180°$ located at $r = 750\,\text{mm}$.
- AGS (PAX): 4 detectors at $\phi = 45°, 135°, 225°, 315°$ located at $r = 85\,\text{mm}$.
- $\Rightarrow$ The AGS geometry provides a greatly enhanced detector solid angle.

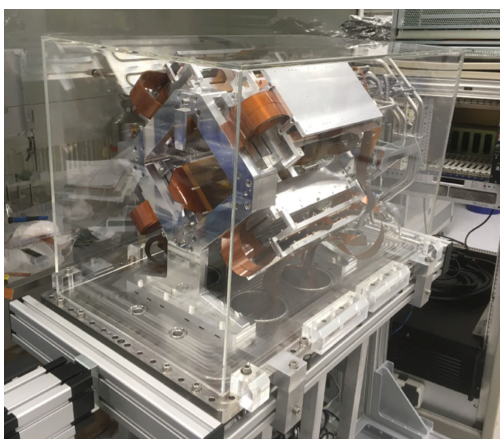

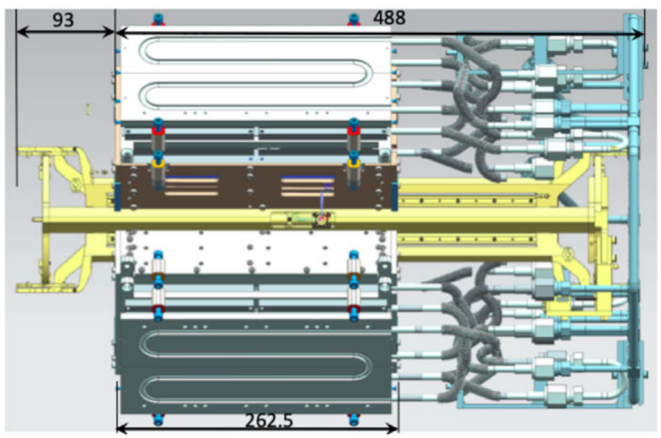

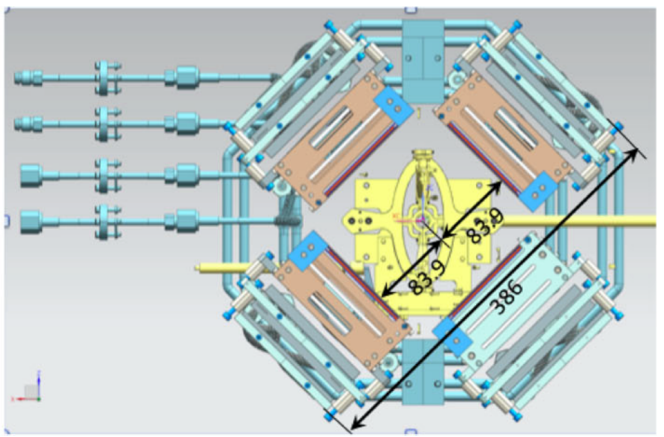

PAX detector system used at COSY [16]. Four detector modules surround the beam axis and provide large azimuthal coverage, and illustrate geometry considered for an AGS storage-cell polarimeter.

Storage cell based polarimetry in the AGS

Polarized internal target at COSY

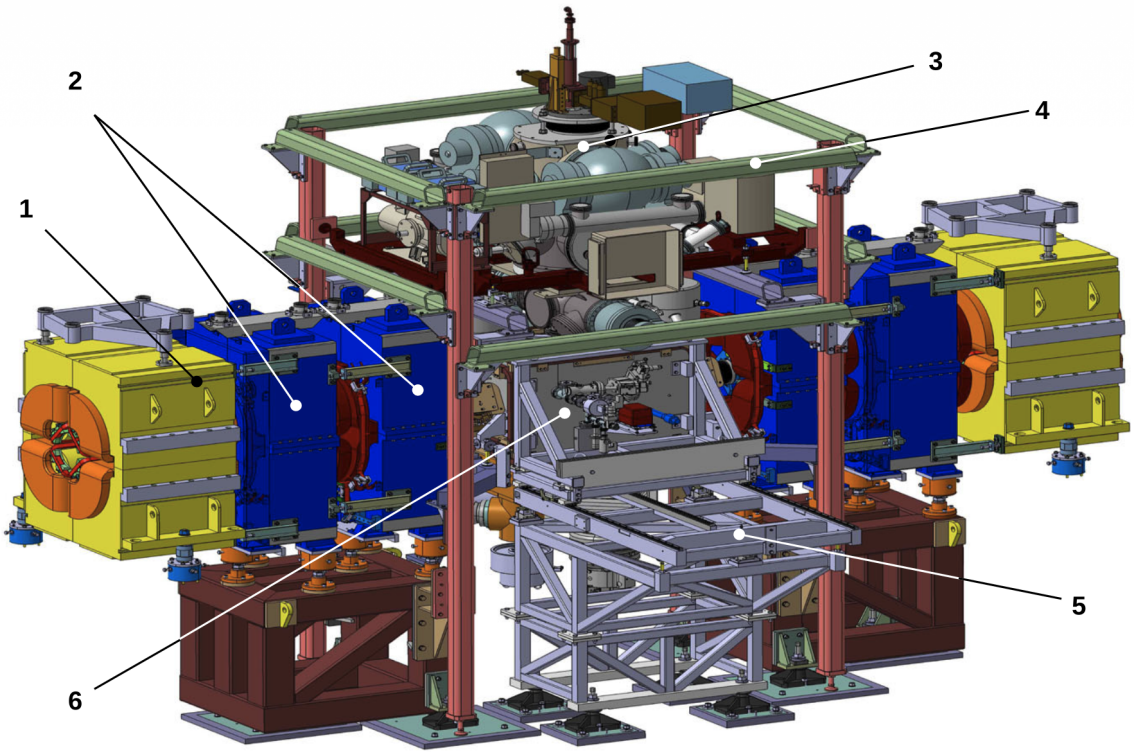

Internal target [16]: 1: quadrupole magnets(1, 2); ABS (3); support system (4); flange supporting rail system (5); target chamber with storage cell (6). BRP and target-gas analyzer (TGA) towards outside of ring.

Storage cell-based polarimetry in the AGS

Target chamber

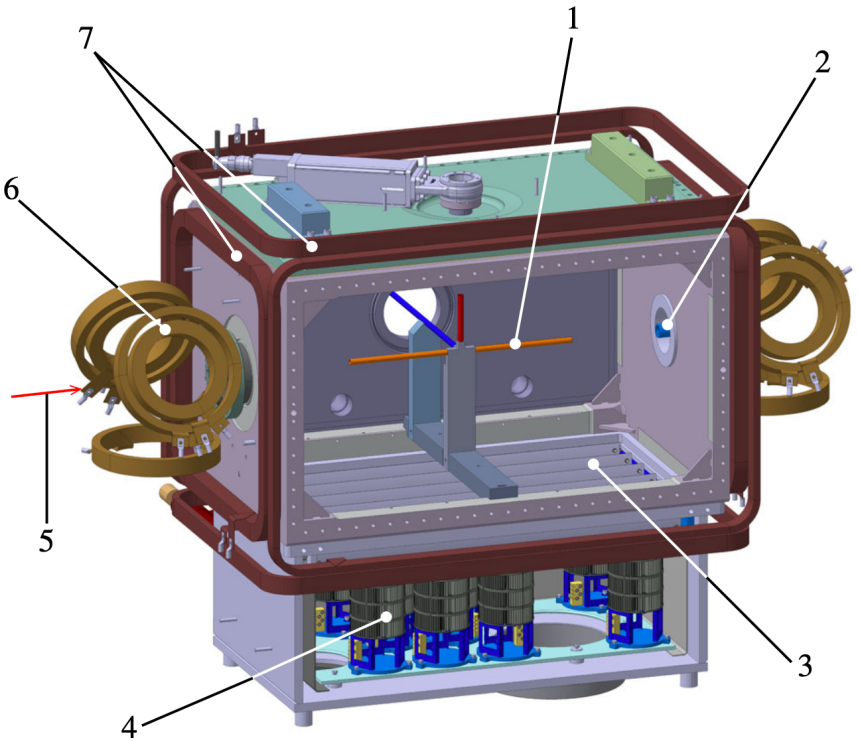

Target chamber [16]: Storage cell (1) with feeding tube to ABS (vertical), extraction tube to BRP, flow limiters (2) of 19 mm diameter and 80 mm length, jalousie (3) to protect cell from heat radiation during activation of nonevaporable getter (NEG) pumps (4), COSY beam (5), guide-field compensation coils (6), magnetic guide-field coils (7).

Storage cell-based polarimetry in the AGS

Target chamber [17]

- NEG pumping system beneath chamber consists of battery of 10 NEG cartridges in a dedicated housing. During activation at 450 °C, mechanical shutter isolates pump to keep chamber temperature below 80 °C.
- With calibrated H_2 inlet, pumping speed of $S = 12\,000\,\mathrm{L\,s^{-1}}$ was measured.
- During COSY operation, the NEG getter pump achieves:
  - base pressure in 10^{-10} mbar range (without ABS gas load),
  - pressure in low 10^{-8} mbar range (ABS injection 3×10^{16} atoms/s, state $|1\rangle$)
- Three orthogonal Helmholtz-coil pairs provide magnetic holding fields in x, y, and z to define quantization axis. Coils mounted along edges of chamber.

Storage cell-based polarimetry in the AGS

Estimate of achievable rate and required target density

- **Beam current** (from slide 58)

$$I_{\text{avg}} = N_{\text{p}}\, N_{\text{b}}\, e\, f_{\text{rev}}, \qquad I_{\text{avg}}^{\text{EIC}} = 1.003\,\text{A}, \qquad I_{\text{avg}}^{\text{RHIC}} = 0.301\,\text{A} \tag{6}$$

- **Event rate**

$$N_{\text{evt}} \propto N_{\text{p}}\, N_{\text{b}}\, d_t\, f_{\text{rev}}\, t\, \Omega_{\text{det}} \tag{7}$$

- **Target density**
  - Reference value is RHIC HJET areal target density $d_t^{\text{RHIC}} = 10^{12}$ atoms/cm^2.
  - Statistical benchmark $\Delta P/P \approx 3\%$ in reference time $t_{\text{RHIC}} = 4\,\text{h}$
  - AGS density required to reach same statistical precision obtained by scaling

$$d_t^{\text{AGS}} = d_t^{\text{RHIC}} \left(\frac{N_{\text{p}}^{\text{RHIC}}}{N_{\text{p}}^{\text{AGS}}}\right) \left(\frac{N_{\text{b}}^{\text{RHIC}}}{N_{\text{b}}^{\text{AGS}}}\right) \left(\frac{t_{\text{RHIC}}}{t_{\text{AGS}}}\right) \left(\frac{\Omega_{\text{RHIC}}}{\Omega_{\text{AGS}}}\right) \tag{8}$$

- **Detector solid-angle ratio** The much larger acceptance of the PAX geometry at the AGS enters through the ratio

$$\frac{\Omega_{\text{AGS}}}{\Omega_{\text{RHIC}}} \simeq \frac{4}{2}\left(\frac{750}{85}\right)^2 \approx 1.6 \times 10^2 \tag{9}$$

Feasibility of storage-cell polarimetry in the AGS

What is achievable?

- With a storage-cell target and large solid-angle detector geometry, *pp* elastic CNI polarimetry at AGS can reach
  - $\Delta P/P \approx 3\%$ in $t_{\mathrm{AGS}} = 5\,\mathrm{min}$, compared to 4 h at RHIC with HJET
  - Target densities required for this:

$$\begin{aligned} d_t^{\mathrm{AGS}}(N_{\mathrm{b}}^{\mathrm{AGS}} = 1) &\approx 3.7 \times 10^{13}\,\mathrm{atoms/cm^2} \\ d_t^{\mathrm{AGS}}(N_{\mathrm{b}}^{\mathrm{AGS}} = 4) &\approx 9.3 \times 10^{12}\,\mathrm{atoms/cm^2}. \end{aligned} \tag{10}$$

- Target densities of $\approx 5 \times 10^{14}\,\mathrm{atoms/cm^2}$ have been used in storage rings, in particular with a powerful NEG-based pumping system. For $\Delta P/P = 3\%$, the required measurement times then become
  - 1 bunch: $t \approx 22\,\mathrm{s}$ and 4 bunches: $t \approx 5.6\,\mathrm{s}$.
- 2 µm Teflon cell wall compatible with requirements, see slide 93.

Key capability at the AGS

A storage-cell target at the AGS could provide fast, high-precision, and energy-resolved polarization measurements during the ramp.

Conclusion and Outlook

Conclusions: Critical technical developments

Solved challenges

1. **HJET** EIC's tenfold increase in bunch frequency creates **electromagnetic harmonics that resonantly drive hyperfine transitions** in hydrogen atoms at RHIC's HJET holding field of 120 mT.
   - 400 mT guide field $\Rightarrow$ transitions shifted above populated harmonics (see [1]).
2. **pC targets**
   - **Target heating:** Larger beam sizes at the pC location at EIC reduce areal power density; thermal modeling $\Rightarrow T_{\text{max}} < T_{\text{sub}}$
   - **Wake fields: dielectric holders** (e.g. Al_2O_3) with 10 nm Au coating (charge control) significantly lower wake impedance vs. metallic designs.

Outlook: Ongoing developments

Ongoing developments

1. **HJET holding-field system:** engineer magnet + chamber; assess compensation for $\int B_{x,y,z}\, d\ell$; preserve vector B_x, B_y, B_z option.
2. **HJET detector system:** increased azimuthal coverage/segmentation to access (P_x, P_y, P_z); track recoils in measured guide-field (see slide 15).
3. **HJET H_2 systematics:** typical ABS H_2 at target 3 % to 4 % $\Rightarrow$ integrate QMA into BRP to accurately determine and monitor H_2 fraction;
4. **Bunch-by-bunch polarimetry:** enable detector/readout to resolve 11 ns spacing (fast Si or diamond; bunch-synchronous timing).
5. **pC target thermal validation:** direct target temperature measurements during beam (RHIC) and extension to IP6 conditions.
6. **pC vacuum transfer chamber:** enable target swaps without breaking ring vacuum; reduce contamination and downtime.
7. **^{3}He targets for absolute beam polarimetry at EIC:**
   - Cryogenic ^{3}He ABS at 1 K (developed at MIT)
   - Laser-driven ^{3}He gas target $\Rightarrow$ significantly higher target densities

   both aligned with early EIC light-ion operation

Outlook: Potential developments

Future developments

1. **Storage-cell internal target in AGS**, based on proven technology, enables fast, energy-resolved *pp* CNI polarimetry during 3 GeV to 23.5 GeV ramp.
2. **Large solid-angle detector** geometry together with thin (2 µm) PTFE storage-cell walls supports fast measurements at higher target densities:
   - **Achievable target densities** $d_t \sim 1 \times 10^{13}$ to few 10^{14} atoms/cm^2
   - With 1 bunch in AGS, time to reach $\Delta P/P \approx 3\,\%$ improves dramatically, compared to 4 h at RHIC (120 bunches, HJET):
     - ≈ 5 min with $d_t = 3.7 \times 10^{13}$ atoms/cm^2
     - ≈ 22 s with $d_t = 5 \times 10^{14}$ atoms/cm^2

Impact for AGS → RHIC → EIC Polarization Control

Proposed capability would significantly strengthen injection polarization control at EIC by enabling continuous polarization measurements throughout AGS ramp

Thank you

I'm happy to take questions

References I

[1] F. Rathmann et al., "Eliminating beam-induced depolarizing effects in the hydrogen jet target for high-precision proton beam polarimetry at the electron-ion collider," (2025), URL https://arxiv.org/abs/2508.01366.

[2] M. Diermaier, C. B. Jepsen, B. Kolbinger, C. Malbrunot, O. Massiczek, C. Sauerzopf, M. C. Simon, J. Zmeskal, and E. Widmann, "In-beam measurement of the hydrogen hyperfine splitting and prospects for antihydrogen spectroscopy," Nature Commun. **8**, 5749 (2017), 1610.06392.

[3] A. Airapetian, N. Akopov, Z. Akopov, M. Amarian, A. Andrus, E. Aschenauer, W. Augustyniak, R. Avakian, A. Avetissian, E. Avetissian, et al., "The hermes polarized hydrogen and deuterium gas target in the hera electron storage ring," Nuclear Instruments and Methods in Physics Research Section A: Accelerators, Spectrometers, Detectors and Associated Equipment **540**, 68 (2005), ISSN 0168-9002, URL https://www.sciencedirect.com/science/article/pii/S0168900204024167.

[4] F. Rathmann, B. von Przewoski, W. A. Dezarn, J. Doskow, M. Dzemidzic, W. Haeberli, J. G. Hardie, B. Lorentz, H. O. Meyer, P. V. Pancella, et al., "Complete angular distribution measurements of pp spin correlation parameters A_{xx}, A_{yy}, and A_{xz} and analyzing power A_y at 197.4 mev," Phys. Rev. C **58**, 658 (1998), URL https://link.aps.org/doi/10.1103/PhysRevC.58.658.

[5] B. von Przewoski et al., "Proton proton analyzing power and spin correlation measurements between 250-MeV and 450-MeV at $7^\circ \leq \theta(c.m.) \leq 90^\circ$ with an internal target in a storage ring," Phys. Rev. C **58**, 1897 (1998).

[6] B. von Przewoski, H. O. Meyer, P. V. Pancella, S. F. Pate, R. E. Pollock, T. Rinckel, F. Sperisen, J. Sowinski, W. Haeberli, W. K. Pitts, et al., "Absolute measurement of the p+p analyzing power at 183 mev," Phys. Rev. C **44**, 44 (1991), URL https://link.aps.org/doi/10.1103/PhysRevC.44.44.

[7] G. Plattner and A. Bacher, "Absolute calibration of spin-$\frac{1}{2}$ polarization," Physics Letters B **36**, 211 (1971), ISSN 0370-2693, URL https://www.sciencedirect.com/science/article/pii/0370269371900712.

References II

[8] P. Blümler and H. Soltner, "Practical Concepts for Design, Construction and Application of Halbach Magnets in Magnetic Resonance," Applied Magnetic Resonance **54**, 1701 (2023), ISSN 1613-7507, URL https://doi.org/10.1007/s00723-023-01602-2.

[9] H. Soltner and P. Blümler, "Dipolar halbach magnet stacks made from identically shaped permanent magnets for magnetic resonance," Concepts in Magnetic Resonance Part A **36A**, 211 (2010), https://onlinelibrary.wiley.com/doi/pdf/10.1002/cmr.a.20165, URL https://onlinelibrary.wiley.com/doi/abs/10.1002/cmr.a.20165.

[10] H. Raich and P. Blümler, "Design and construction of a dipolar halbach array with a homogeneous field from identical bar magnets: Nmr mandhalas," Concepts in Magnetic Resonance Part B: Magnetic Resonance Engineering **23B**, 16 (2004), https://onlinelibrary.wiley.com/doi/pdf/10.1002/cmr.b.20018, URL https://onlinelibrary.wiley.com/doi/abs/10.1002/cmr.b.20018.

[11] K. Abe, K. Tadakuma, and R. Tadakuma, "Abenics: Active ball joint mechanism with three-dof based on spherical gear meshings," IEEE Transactions on Robotics **37**, 1806 (2021).

[12] M. E. M. Stewart, Tech. Rep. NASA/TM-2015-218987, NASA (2015), states: "graphite sublimes at 3915 K", URL https://ntrs.nasa.gov/api/citations/20150002852/downloads/20150002852.pdf.

[13] P. Thieberger, "Polarimeter target beam heating simulation version 4,", Private communication (2025), unpublished Excel-based thermal simulation code, version 27.09.2025, available upon request.

[14] D. DeSchepper et al., "The hermes polarized ^{3}he internal gas target," Nuclear Instruments and Methods in Physics Research Section A **419**, 16 (1998).

[15] M. Capiluppi, V. Carassiti, G. Ciullo, et al., "Dual H and D cavity for the PAX target polarimeter," Physics of Particles and Nuclei **45**, 283 (2014), DOI link, URL https://doi.org/10.1134/S1063779614010171.

References III

[16] P. Lenisa, F. Rathmann, L. Barion, S. Barsov, S. Bertelli, V. Carassiti, G. Ciullo, M. Contalbrigo, A. C. Ramusino, S. Dymov, et al., "Low-energy spin-physics experiments with polarized beams and targets at the cosy storage ring," EPJ Techniques and Instrumentation **6**, 2 (2019), ISSN 2195-7045, URL https://doi.org/10.1140/epjti/s40485-019-0051-y.

[17] C. Weidemann, F. Rathmann, H. J. Stein, B. Lorentz, Z. Bagdasarian, L. Barion, S. Barsov, U. Bechstedt, S. Bertelli, D. Chiladze, et al., "Toward polarized antiprotons: Machine development for spin-filtering experiments," Phys. Rev. ST Accel. Beams **18**, 020101 (2015), URL http://link.aps.org/doi/10.1103/PhysRevSTAB.18.020101.

[18] H. Paetz gen. Schieck, *Nuclear Physics with Polarized Particles*, vol. 842 of *Lecture Notes in Physics* (Springer, Berlin, Heidelberg, 2012), ISBN 978-3-642-24225-0.

[19] N. Ramsey, *Molecular Beams* (Oxford University Press, 1956).

[20] H.-O. Meyer, "The Indiana Cooler: a retrospective," Ann. Rev. Nucl. Part. Sci. **57**, 1 (2007).

[21] R. E. Pollock, W. A. Dezarn, M. Dzemidzic, J. Doskow, J. G. Hardie, H. O. Meyer, B. v. Przewoski, T. Rinckel, F. Sperisen, W. Haeberli, et al., "Calibration of the polarization of a beam of arbitrary energy in a storage ring," Phys. Rev. E **55**, 7606 (1997), URL https://link.aps.org/doi/10.1103/PhysRevE.55.7606.

[22] B. v. Przewoski et al., "Analyzing powers and spin correlation coefficients for $p + d$ elastic scattering at 135 and 200 MeV," Phys. Rev. C **74**, 064003 (2006), URL http://link.aps.org/doi/10.1103/PhysRevC.74.064003.

[23] J. Abrahamson, "Graphite sublimation temperatures, carbon arcs and crystallite erosion," Carbon **12**, 111 (1974), concludes one-atmosphere sublimation temperature lies between 3895 and 4020 K.

[24] M. Planck, *The Theory of Heat Radiation* (P. Blakiston's Son & Co., 1914).

References IV

[25] L. Brewer, P. W. Gilles, and F. A. Jenkins, "The vapor pressure and heat of sublimation of graphite," The Journal of Chemical Physics **16**, 797 (1948).

[26] J. R. Haines and C. C. Tsai, Tech. Rep. ORNL/TM-2002/27, Oak Ridge National Laboratory, Oak Ridge, TN (2002), summarizes literature vapor-pressure fits for graphite and maps them to UHV erosion rates via the Hertz–Knudsen relation., URL `https://info.ornl.gov/sites/publications/Files/Pub57715.pdf`.

[27] J. F. O'Hanlon, *A User's Guide to Vacuum Technology* (John Wiley & Sons, Hoboken, NJ, 2003), 3rd ed.

[28] D. Chiladze et al., "Determination of deuteron beam polarizations at cosy," Phys. Rev. ST Accel. Beams **9**, 050101 (2006), URL `http://link.aps.org/doi/10.1103/PhysRevSTAB.9.050101`.

Backup material

Instruments, spare slides

Present RHIC detector system at the polarized jet target

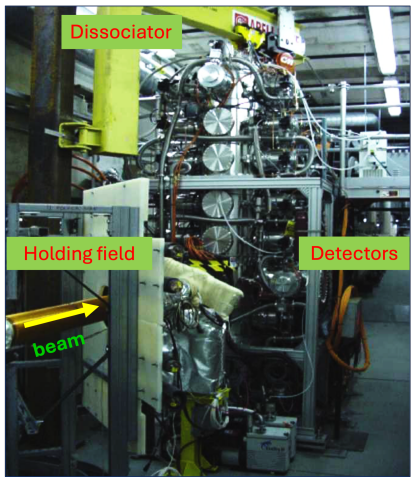

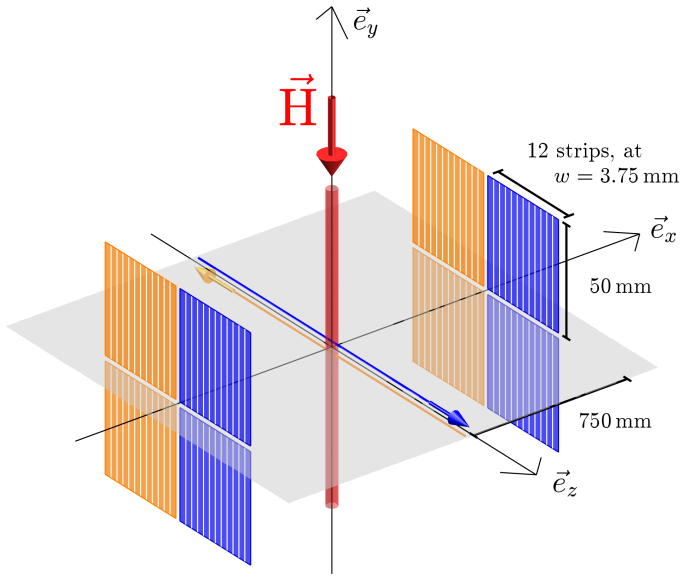

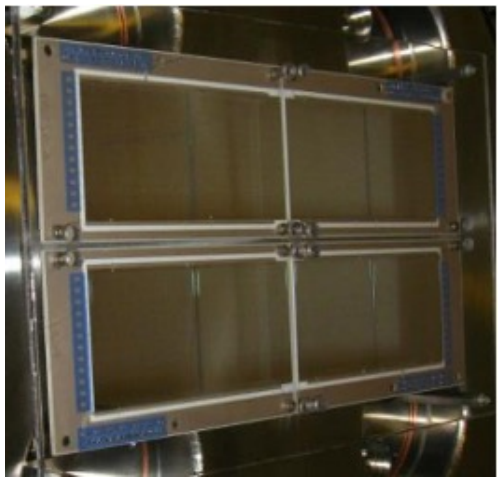

Eight Si strip detectors

- 12 vertical strips, 3.75 mm pitch, 500 µm thickness

With present setup of L-R detectors and guide field B_y

- Only vertical component P_y measurable via L-R asymmetry near $\theta = 90°$.

Present CNI polarimeter setup

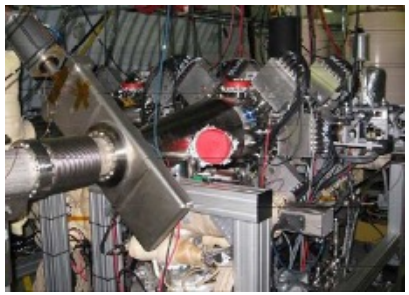

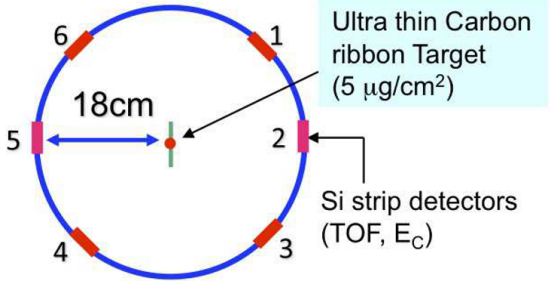

CNI setup with 6 Si detectors at different azimuth at each target enables

- determination of polarization components P_x and P_y
- determination of polarization profile along x and y
- Due to parity violation, $A_z \approx 0$ (no longitudinal analyzing power) $\rightarrow$ P_z not measurable with *unpolarized* target

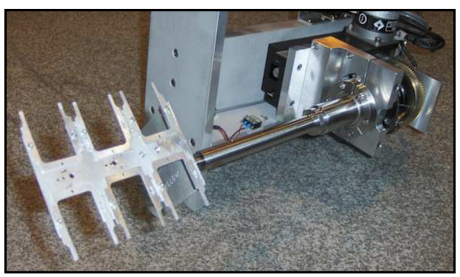

Ultra-thin ribbon targets

- 8 target holder inside beam pipe
- 2 holders per beam for x and y
- 6 targets per holders, 48 in total
- Targets $\approx 10\,\mu\text{m} \times 50\,\text{nm}$, hand crafted by D. Steski & team

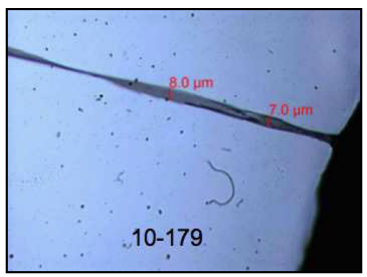

Hydrogen atom, spare slides

Energy levels of the H atom [18]: Not to scale!

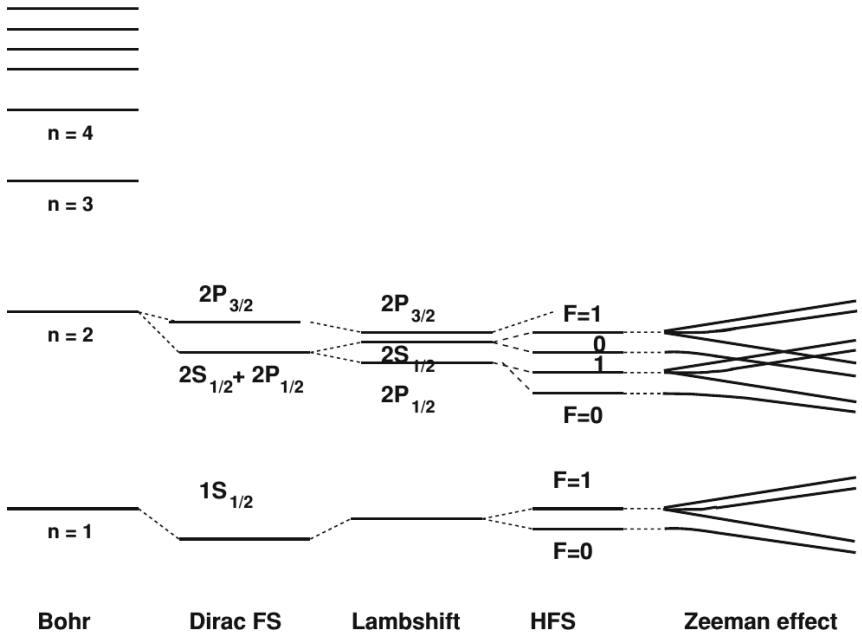

- **Bohr**
  - Electron orbits nucleus
  - Coulomb binding $\sim 13.6\,\text{eV}/n^2$
- **Fine Structure**
  - Electron **spin** $\leftrightarrow$ **orbital motion**
  - Spin-orbit coupling $\sim 10^{-4}\,\text{eV}$
- **Lamb Shift**
  - Electron $\leftrightarrow$ **vac. fluctuations**
  - QED effect $\sim 10^{-6}\,\text{eV}$
- **Hyperfine**
  - Electron $\leftrightarrow$ **nucl.** magn. moment
  - 1420 MHz (21 cm) $\sim 6 \times 10^{-6}\,\text{eV}$
- **Zeeman**
  - Magnetic moments $\leftrightarrow$ **ext. field B**
  - $\sim 10^{-5}\,\text{eV}$ per 0.1 T
  - Used for spin selection in ABS

Critical field for hydrogen hyperfine splitting I

Zeeman region:

- magnetic flux density at which energy separation between different hyperfine levels becomes comparable to Zeeman splitting.
- referred to as *critical magnetic field* or *Breit-Rabi field* B_c
- Breit-Rabi formula (energy levels of hydrogen atom in external magnetic field:

$$E_{F,m_F} = -\frac{E_{\text{hfs}}}{2(2I+1)} + g_J \mu_B m_J B \pm \frac{E_{\text{hfs}}}{2}\sqrt{1 + \frac{2m_F x}{F} + x^2}\,, \text{where} \qquad (11)$$

- E_{hfs} is hyperfine splitting energy
- I is nuclear spin (for H, $I = \frac{1}{2}$)
- g_J is Landé g-factor
- μ_B is Bohr magneton
- m_J is magnetic quantum number
- m_F is total angular momentum quantum number
- $x = \frac{g_J \mu_B B}{E_{\text{hfs}}}$
- $F = I + J$ is total angular momentum (for H, $J = \frac{1}{2}$)

Critical field for hydrogen hyperfine splitting II

For H:

- hyperfine splitting energy E_{hfs} (1420 MHz):

$$E_{\mathrm{hfs}} \approx 5.874 \times 10^{-6}\,\mathrm{eV} \tag{12}$$

- Critical field B_c is when Zeeman energy $g_J \mu_B B$ is comparable to E_{hfs}. With $g_J \mu_B B_c \approx E_{\mathrm{hfs}}$, we get:

$$B_c \approx \frac{E_{\mathrm{hfs}}}{g_J \mu_B} \tag{13}$$

- For H, $g_J \approx 2$ (approximately for electron), and $\mu_B \approx 5.788 \times 10^{-5}\,\mathrm{eV/T}$. Thus,

$$B_c \approx \frac{5.874 \times 10^{-6}\,\mathrm{eV}}{2 \times 5.788 \times 10^{-5}\,\mathrm{eV/T}} \approx 50.7\,\mathrm{mT} \tag{14}$$

Bunch-induced depolarization, spare slides

Hyperfine states of hydrogen

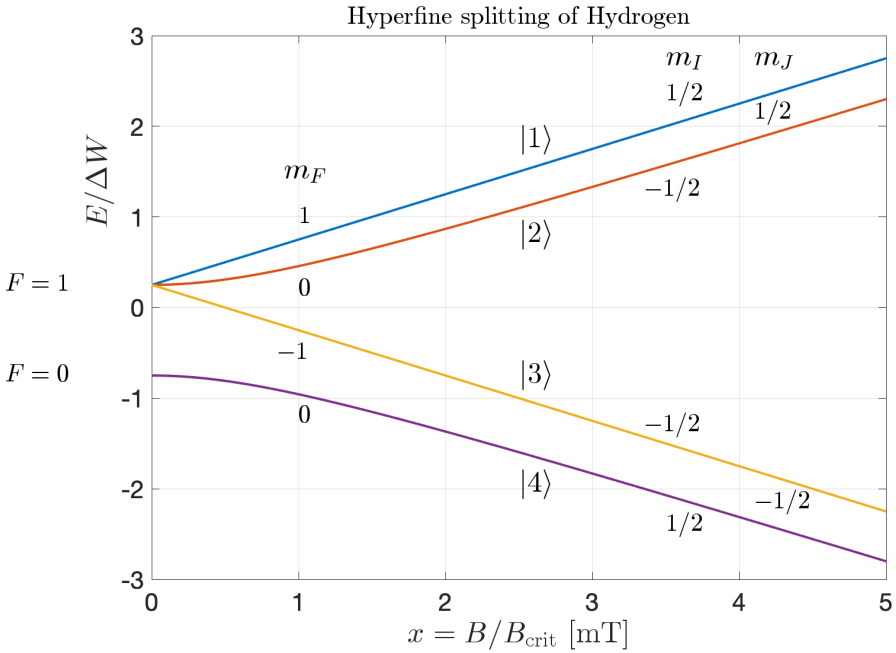

Energy levels of hydrogen (slide 52)

- Zeeman energy $g_J \mu_B B$ comparable to E_{hfs}
- $E_{\mathrm{hfs}} \approx 5.874 \times 10^{-6}\,\mathrm{eV}$ ($\approx$1420 MHz [2]):
- Critical field $B_c = 50.7\,\mathrm{mT}$ (slide 53)

Transition frequencies

- Transition frequency between two hyperfine states $|i\rangle$ and $|j\rangle$ given by:

$$f_{ij} = \frac{E_{|i\rangle}(B) - E_{|j\rangle}(B)}{h} \tag{15}$$

- **When f_{ij} matches one of the beam harmonics at a certain holding field $|\vec{B}|$, resonant depolarization occurs** [3]

Hyperfine transitions in H from bunch fields at RHIC

Depolarization occurs when f_{ij} multiple of bunch frequency f_b^{RHIC}

- HJET injects states $|1\rangle + |4\rangle$ ($p^{\uparrow}$) and $|2\rangle + |3\rangle$ ($p^{\downarrow}$).
  - What is exact magnitude and orientation of $\vec{B}^{\mathrm{HJET}}$? **Visit issue after run 25**

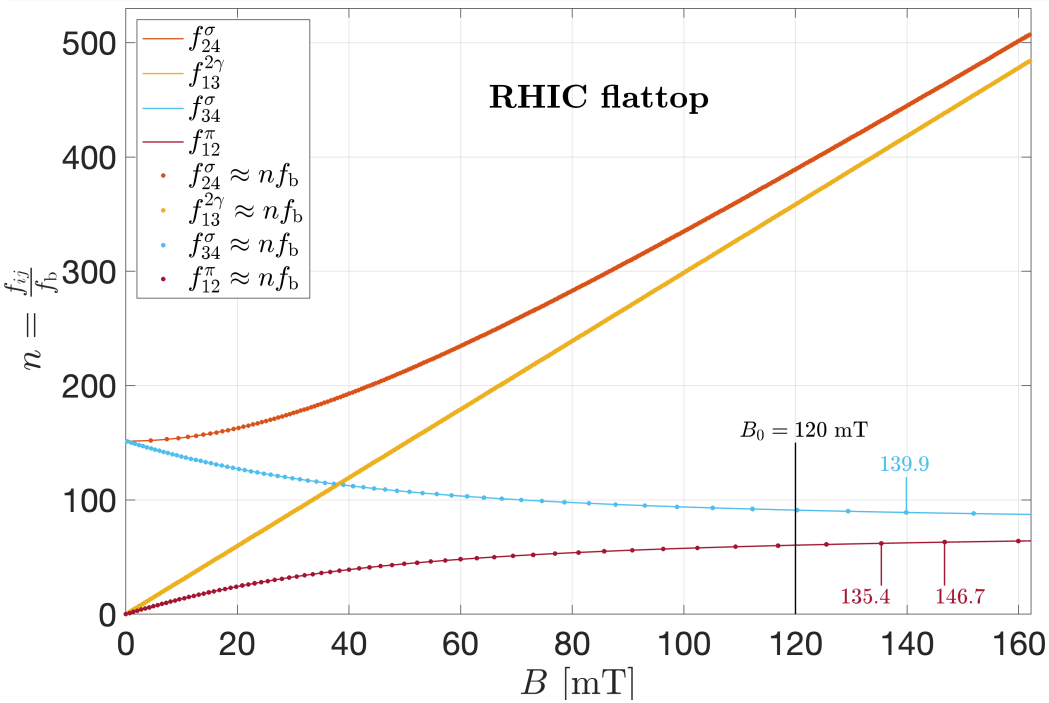

- $f_{ij}(B) \approx n\, f_{\mathrm{b}}^{\mathrm{RHIC}}$, $n \in \mathbb{N}$
- No depolarization from same $m_I \Rightarrow f_{14}^{\sigma}$, f_{23}^{π} omitted

HJET at RHIC operated in safe region around $B_y = 120\,\mathrm{mT}$

- At RHIC, transitions with $\frac{f_{ij}}{f_b^{\mathrm{RHIC}}} \gtrsim 350$ were ignored
- Don't know exactly at which harmonic number, depolarization sets in.

Beam bunch parameters for RHIC and EIC

RHIC and EIC flattop (from [1])

Metric	**RHIC**	**EIC flattop**
Total beam energy E_{beam} [GeV]	255	275
Protons per bunch N_p [10^{10}]	20	6.9
Number of bunches N_b	120	1160
Bunch length σ_L [m]	0.55	0.06
Temporal bunch width σ_t [ns]	1.835	0.200
Bunch spacing τ_b [ns]	106.598	11.027
Revolution frequency [kHz]	78.175	78.175
Bunch frequency f_b [MHz]	9.381	90.683
Beta function (horizontal) β_x [m]	5.340	230.323
Beta function (vertical) β_y [m]	6.190	69.935
Transverse rms beam size (horizontal) σ_x [mm]	0.23	1.610
Transverse rms beam size (vertical) σ_y [mm]	0.23	0.268

Bunch-induced radio-frequency fields at EIC flattop

- Bunch in EIC, $\sigma_t = 0.2\,\text{ns}$
- $\tau_\text{b} = 11.027\,\text{ns}$
- $N_b = 1160$ stored bunches
- $f_\text{b} = 90.683\,\text{MHz}$

- Single-sided amplitude spectrum of FFT

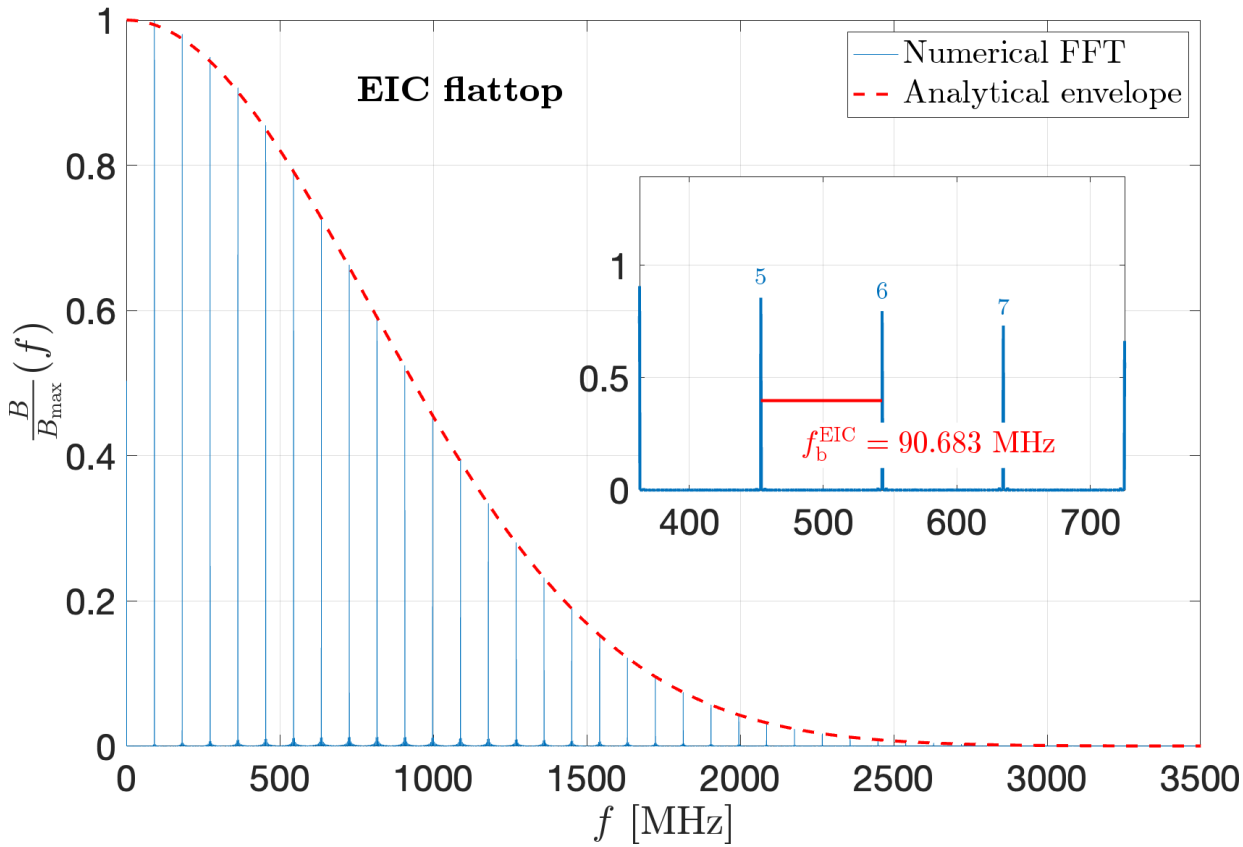

Hyperfine transitions in H from bunch fields at EIC

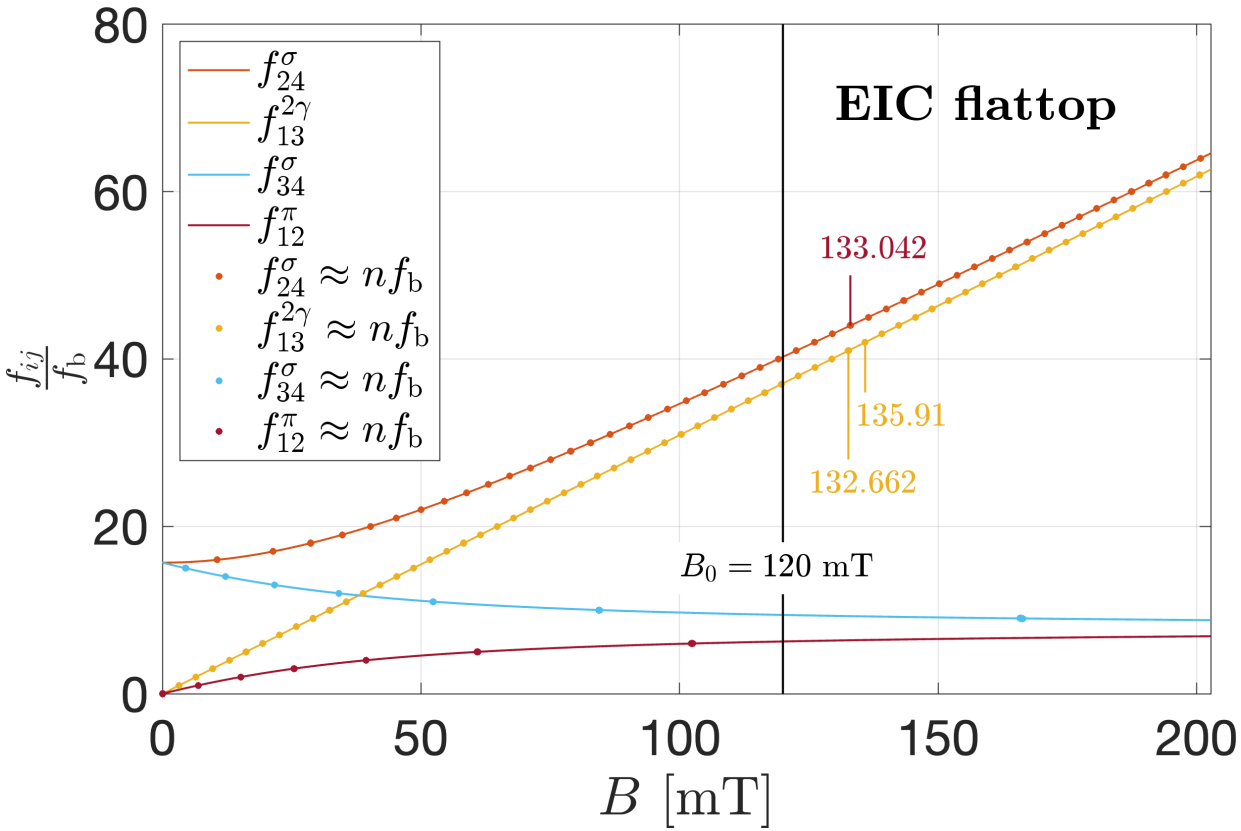

As before, depolarization occurs (numerically) when $f_{ij}(B) \approx n\, f_b^{\mathrm{EIC}}$, $n \in \mathbb{N}$.

In contrast to RHIC, for $B < 120\,\mathrm{mT}$

- **All transitions below harmonic number ≈ 35 would contribute at EIC!**

Single bunch and convolution

- (Gaussian) bunch in RHIC

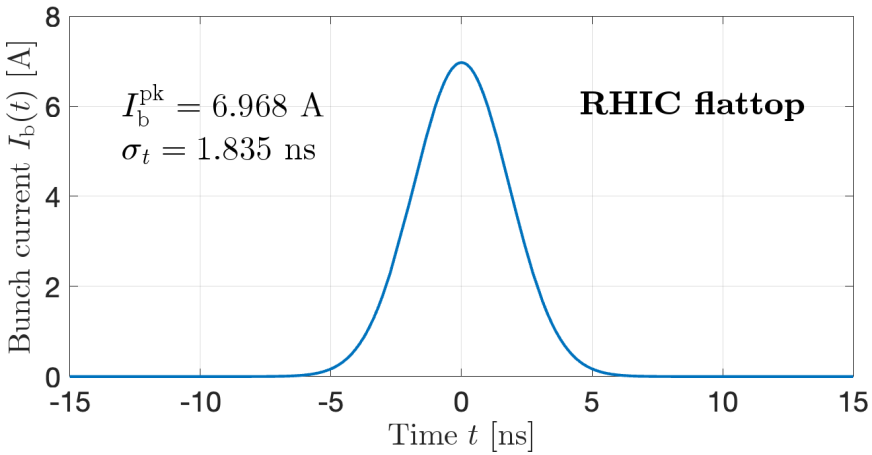

Pulse shape described by

$$f(t) = \frac{Q}{\sqrt{2\pi}\sigma_t} \exp\left(-\frac{t^2}{2\sigma_t^2}\right) \quad (16)$$

- Gaussian convoluted with (finite) series of delta functions.

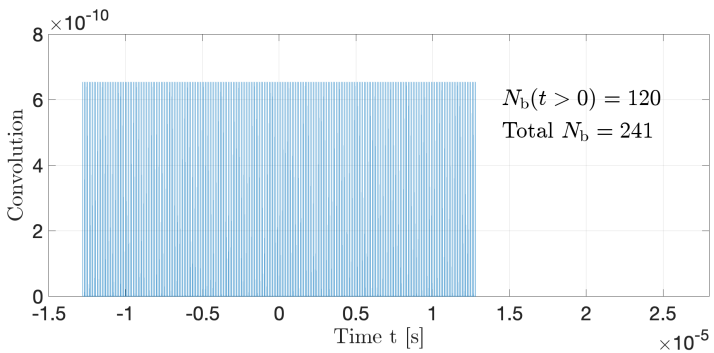

Total beam current as function of time t

$$I(t) = \int_{-\infty}^{\infty} f(t-\xi) \sum_{k=-\infty}^{\infty} \delta\left(\xi - k\frac{\tau_{rev}}{N_b}\right) d\xi \quad (17)$$

Produced radio-frequency fields from FFT of convolution

- Single-sided amplitude spectrum of FFT
- x-axis converted to frequency

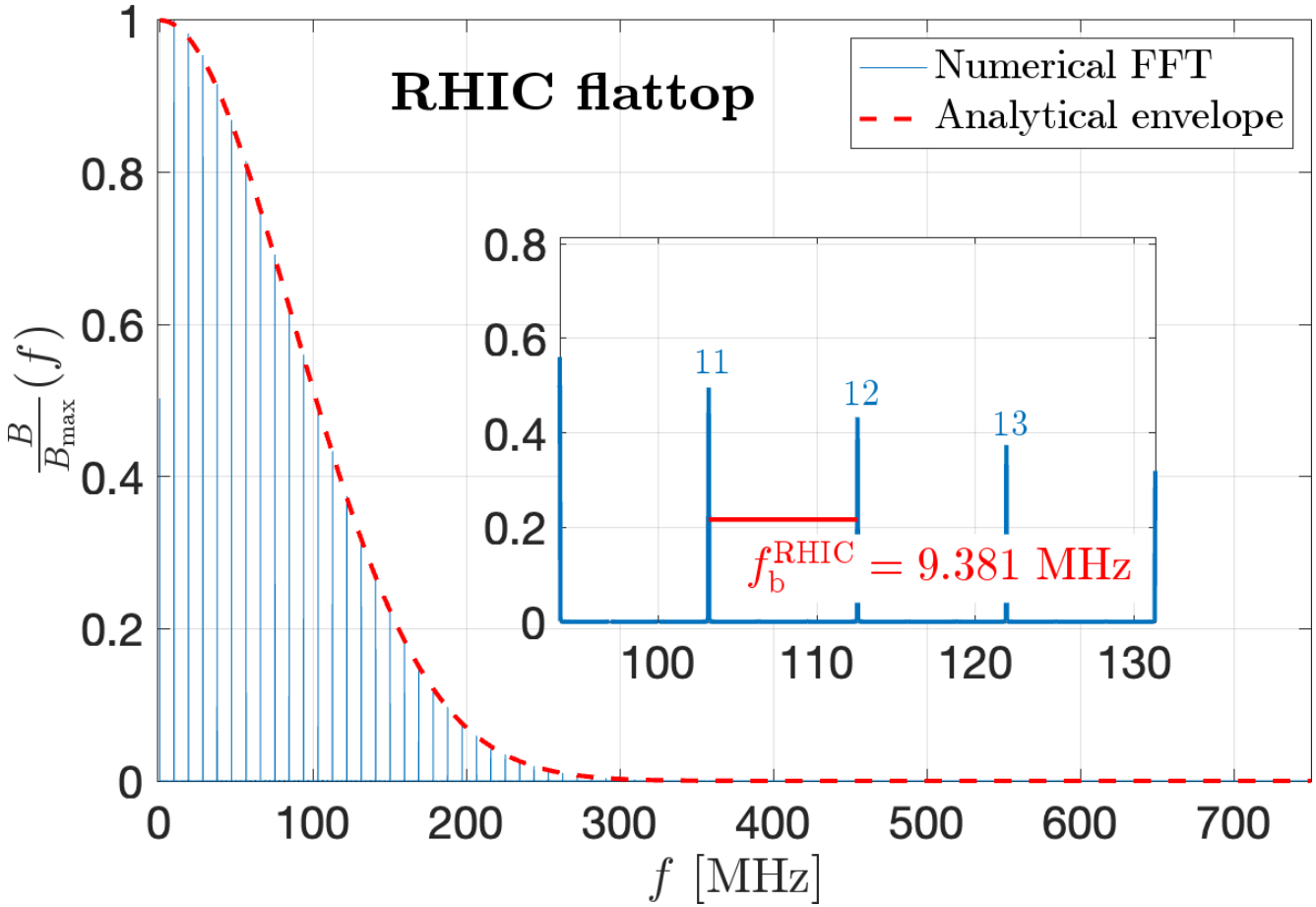

Transition frequencies between hyperfine states of H

Using Zeeman splitting (see slide 56, Eq. (15))

- $\vec{B}_0$ is the static guiding field; $\vec{B}_1(t)$ is the RF field.
- Magnetic–moment precession of $\vec{\mu}$ about $\vec{B}_{\text{tot}}$

$$\frac{\mathrm{d}\vec{s}}{\mathrm{d}t} = \vec{\mu} \times \vec{B}_{\text{tot}} \tag{18}$$

- Adiabatic fast passage commonly used in ABS operation.
- Determine transition frequencies f_{ij} between states $|i\rangle$ and $|j\rangle$.
- **Selection rules** (quantization axis $\vec{e}_z \parallel \vec{B}_0$ [18, 19]):
  - π **transitions** ($\vec{B}_1 \perp \vec{B}_0$):
    - Weak field ($B_0 \ll B_{\text{crit}}$): $\Delta F = 0, \quad \Delta m_F = \pm 1$
    - Strong field ($B_0 \gg B_{\text{crit}}$): $\Delta m_J = \pm 1, \quad \Delta m_I = 0$
  - σ **transitions** ($\vec{B}_1 \parallel \vec{B}_0$):
    - Weak field: $\Delta F = \pm 1, \quad \Delta m_F = 0, \pm 1 \quad (F{=}0 \nleftrightarrow F{=}0)$
    - Strong field: $\Delta m_J = 0, \quad \Delta m_I = 0, \pm 1$

Transition frequencies between hyperfine states of H

Possible transitions

- Single photon transitions in H: f_{12}^{π}, f_{23}^{π}, f_{14}^{σ}, f_{24}^{σ}, and f_{34}^{σ}.
- Transition $f_{13}^{2\gamma}$ with $\Delta m_F = 2$ requires two photons.

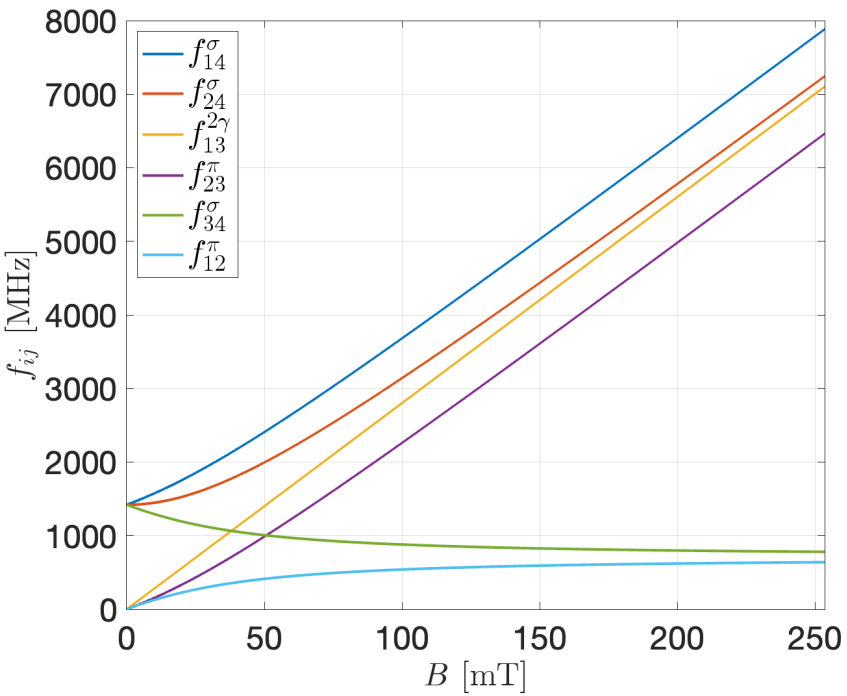

- For $n = 4$ hyperfine states, $\binom{n}{2} = 6$ transitions possible.
- f_{14}^{σ} and f_{23}^{π} transitions leave m_I unchanged $\Rightarrow$ don't affect nuclear polarization.

Polarization components, detector symmetry, spare slides

Polarization of beam $\vec{P}$ and target $\vec{Q}$ [4, 5]

- From measurements at the Indiana Cooler [20]

	$\pm x$		$\pm y$		$\pm z$	
	PRE	POST	PRE	POST	PRE	POST
P_x	0.0052(47)	0.0089(44)	0.0052(47)	0.0089(44)	0.0052(47)	0.0089(44)
P_y [a]	**0.5801(34)**	**0.5425(32)**	**0.5802(34)**	**0.5417(32)**	**0.5765(34)**	**0.5447(32)**
P_z	−0.0021(47)	0.0003(44)	−0.0021(47)	0.0003(44)	−0.0021(47)	0.0003(44)
Q_x	**0.7401(59)**	**0.7394(56)**	−0.0039(59)	0.0039(56)	−0.0071(23)	−0.0052(23)
Q_y	0.0111(59)	0.0039(56)	**0.7400(59)**	**0.7406(56)**	−0.0055(59)	−0.0034(56)
Q_z	0.0158(60)	0.0240(60)	−0.0174(61)	−0.0121(61)	**0.7401(42)** [b]	**0.7400(40)** [b]
S_{P_y}	−0.0008(18)	−0.0005(17)	−0.0008(18)	0.0005(17)	−0.0008(18)	0.0005(17)
S_{Q_x}	0.0017(23)	−0.0007(23)	−0.0040(23)	−0.0031(23)	−0.0043(23)	−0.0024(23)
S_{Q_z}	−0.0091(82)	−0.0162(82)	−0.0177(82)	−0.0197(82)	0.0013(82)	−0.0086(82)

- Beam polarization export/calibration to arbitrary energy [21]
  - PRE ≡ b (197.4 MeV)
  - Export ≡ c (399.1 MeV)
  - POST ≡ d (197.4 MeV)

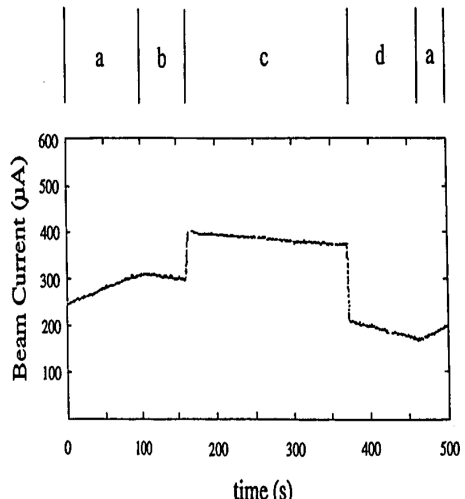

Detector symmetry required to accomplish the task

For spin $\frac{1}{2}$ + spin $\frac{1}{2}$ scattering, suitable geometry below shows pattern of detected azimuthal angles [4].

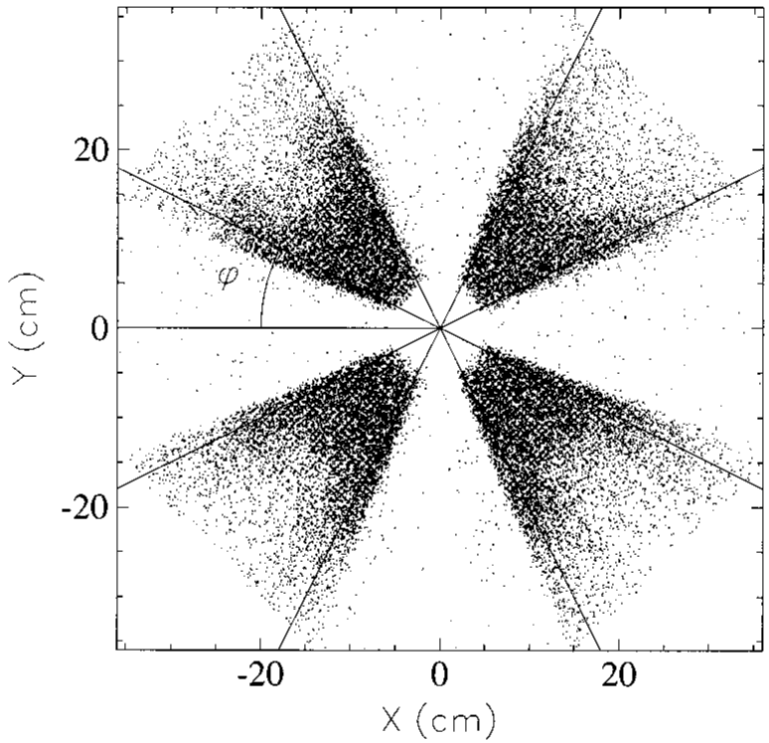

For spin $\frac{1}{2}$ + spin 1 scattering, a higher segmentation is needed, because besides $\sin\phi$ and $\sin 2\phi$, also terms $\sin 3\phi, \ldots$ contribute to asymmetries [22].

Holding field system, spare slides

Technical realization

LDRD C application

With properly rotated spheres

- Setup allows for azimuthally symmetric detector setup with acceptance $\Delta\phi \approx \pm 20^\circ$ at $\phi = 45$, 135, 225, and 315°
  - Slides 67 and 66 show azimuthal acceptance could look like
- **Technical challenges:**
  1. Accurate 3D reorientation of magnetized spheres[a] in vacuum [11]
  2. Vacuum compatible coating, like Ni, or stainless steel covers to prevent H and H_2 from deteriorating NeFeB
  3. **First Step: build a lab test setup and verify concept is technically sound**
  4. Forces and torques appear manageable (see slide 73)

[a] https://www.youtube.com/watch?v=hhDdfiRCQS4

Component $B_x(O)$ using two sets of $\vec{m}$'s

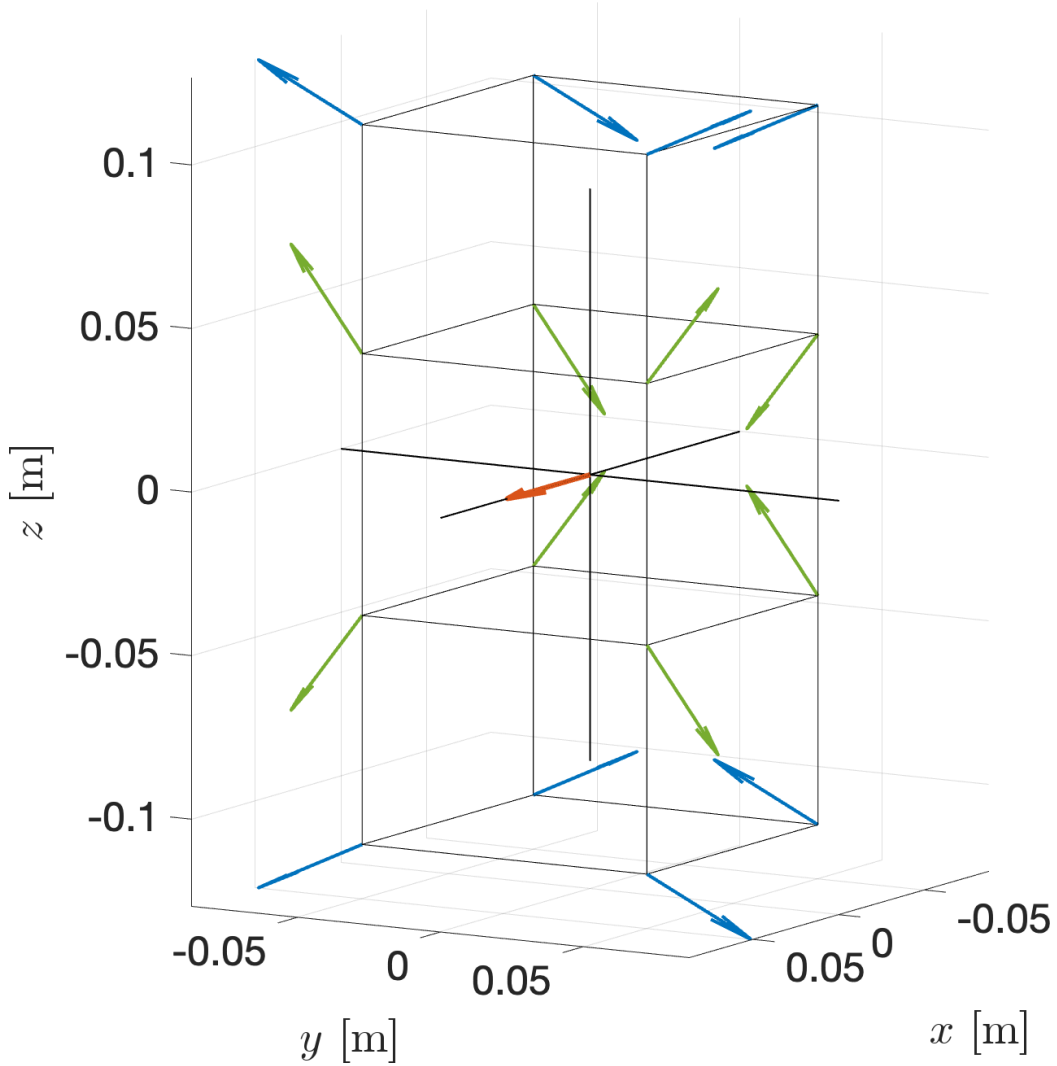

$$B_x: \begin{pmatrix} 0.3224 \\ 0 \\ 0 \end{pmatrix} \text{T}$$

Component $B_y(O)$ using two sets of $\vec{m}$'s

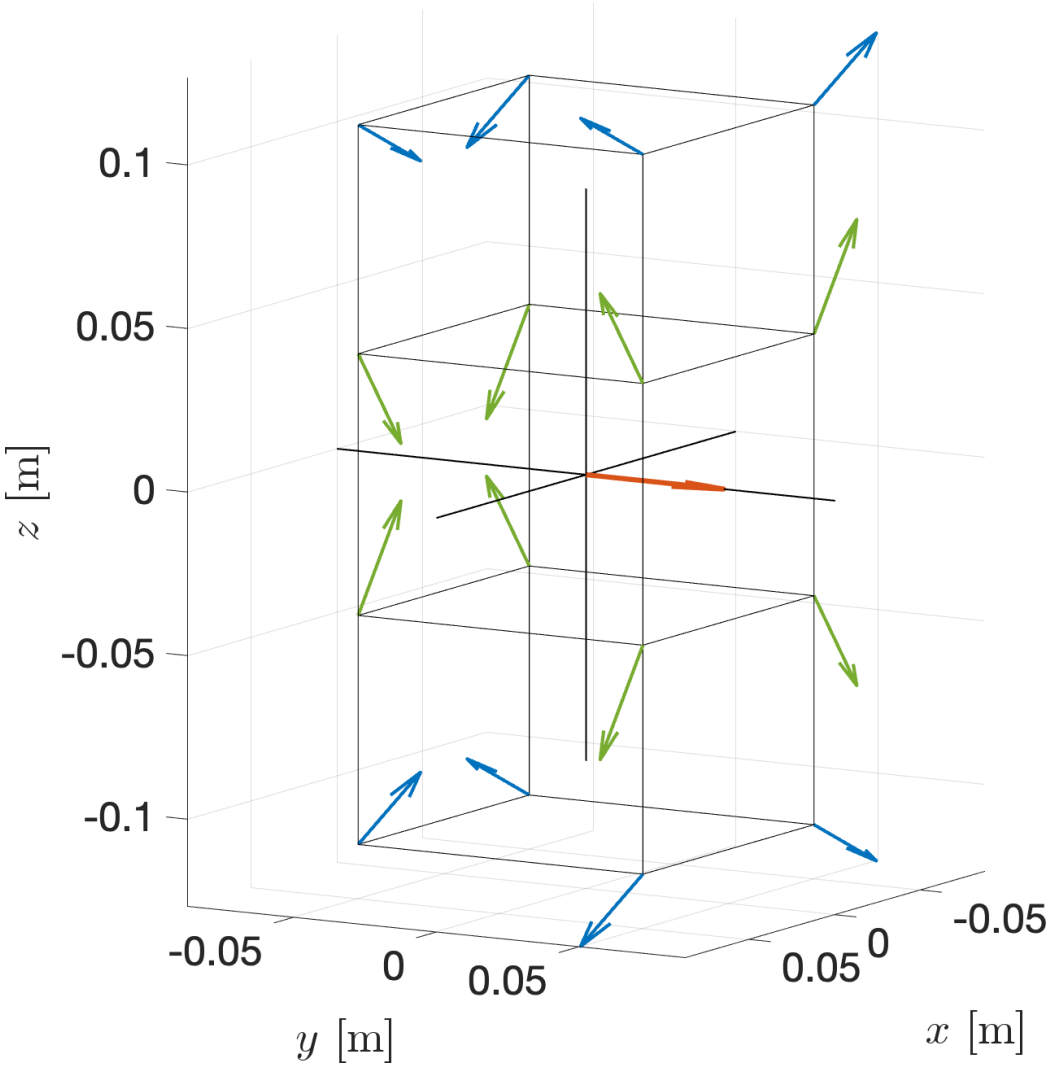

$$B_y: \begin{pmatrix} 0 \\ 0.3224 \\ 0 \end{pmatrix} \text{T},$$

Component $B_z(O)$ using two sets of $\vec{m}$'s

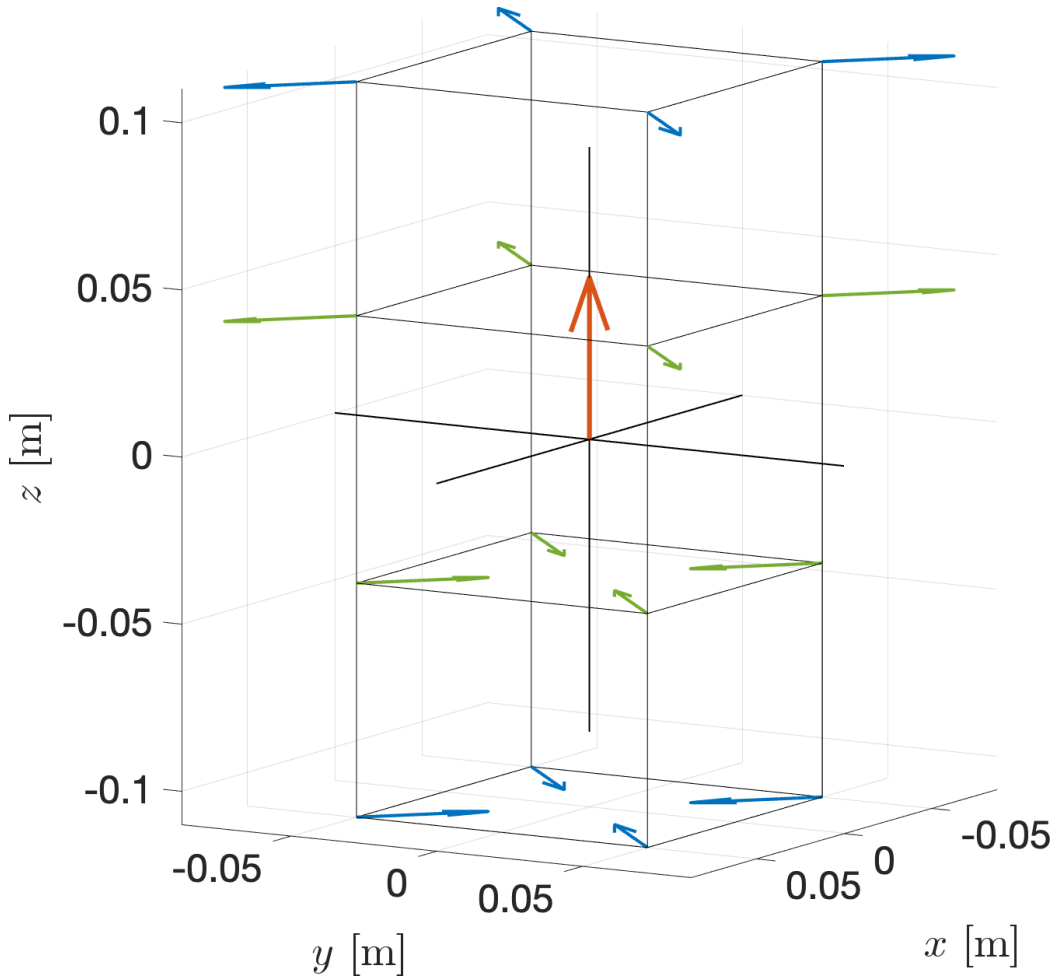

$$B_z: \begin{pmatrix} 0 \\ 0 \\ 0.3227 \end{pmatrix} \text{T}$$

Force and torque between magnetic dipoles $\vec{m}_1$ and $\vec{m}_2$ I

Potential energy of magnetic dipole

$$U = -\vec{m} \cdot \vec{B}$$
$$\vec{F} = -\vec{\nabla} U \quad \rightarrow \quad F_{12} = \vec{\nabla}\left(\vec{m}_2 \cdot \vec{B}_1\right) \tag{19}$$

- $\vec{B}_1$ is flux density produced by $\vec{m}_1$ at location of $\vec{m}_2$.

Force:

$$\vec{F}_{12}(\vec{r}_{12}, \vec{m}_1, \vec{m}_2) = \frac{3\mu_0}{4\pi r_{12}^4}\Big[\vec{m}_2\left(\vec{m}_1 \cdot \vec{e}_{12}\right) + \vec{m}_1\left(\vec{m}_2 \cdot \vec{e}_{12}\right) + \vec{e}_{12}\left(\vec{m}_1 \cdot \vec{m}_2\right) - 5\vec{e}_{12}\left(\vec{m}_1 \cdot \vec{e}_{12}\right)\left(\vec{m}_2 \cdot \vec{e}_{12}\right)\Big] \tag{20}$$

- $\vec{r}_{12}$ is vector between $\vec{m}_1$ and $\vec{m}_2$, $\vec{e}_{12} = \frac{\vec{r}_{12}}{|r_{12}|}$.

Torque

$$\vec{\tau} = \vec{m}_2 \times \vec{B}_1 \tag{21}$$

Force and torque between magnetic dipoles $\vec{m}_1$ and $\vec{m}_2$ II

Examples: $\vec{m}_1 \perp \vec{m}_2$

1. Spheres touch:

$$r_{12} = 0.06\,\mathrm{m} \quad \vec{F}_{12} = -417\,\mathrm{N} \quad \tau_{12} = 8.3\,\mathrm{Nm} \tag{22}$$

2. System assembled:

$$r_{12} \geq 0.07\,\mathrm{m} \quad \vec{F}_{12} \leq -225\,\mathrm{N} \quad \tau_{12} = 5.2\,\mathrm{Nm} \tag{23}$$

Flux density of system in 3D

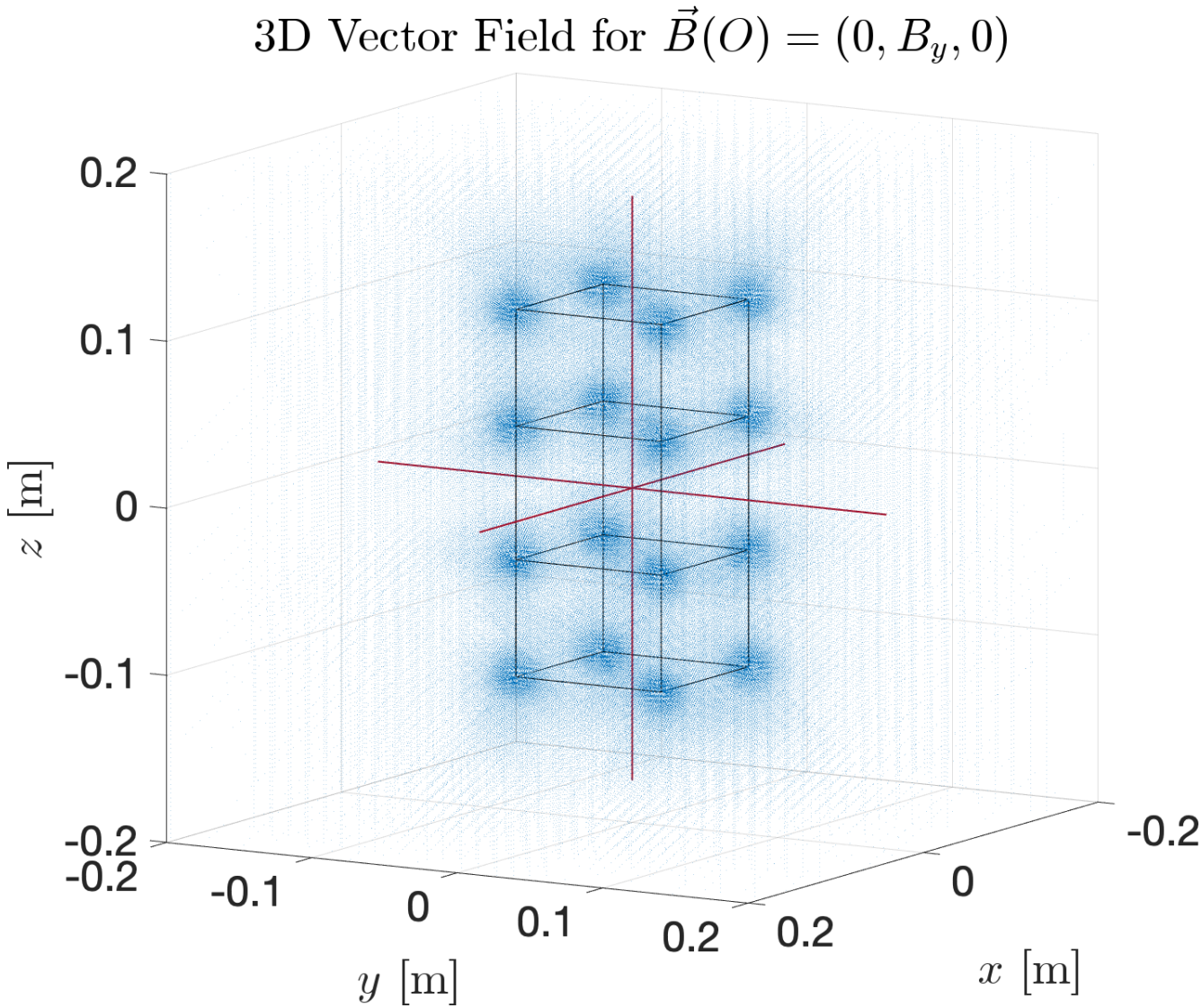

No zero crossings along axes

$\vec{B}(O) \parallel \vec{e}_x$

$\vec{B}(O) \parallel \vec{e}_y$

$\vec{B}(O) \parallel \vec{e}_z$

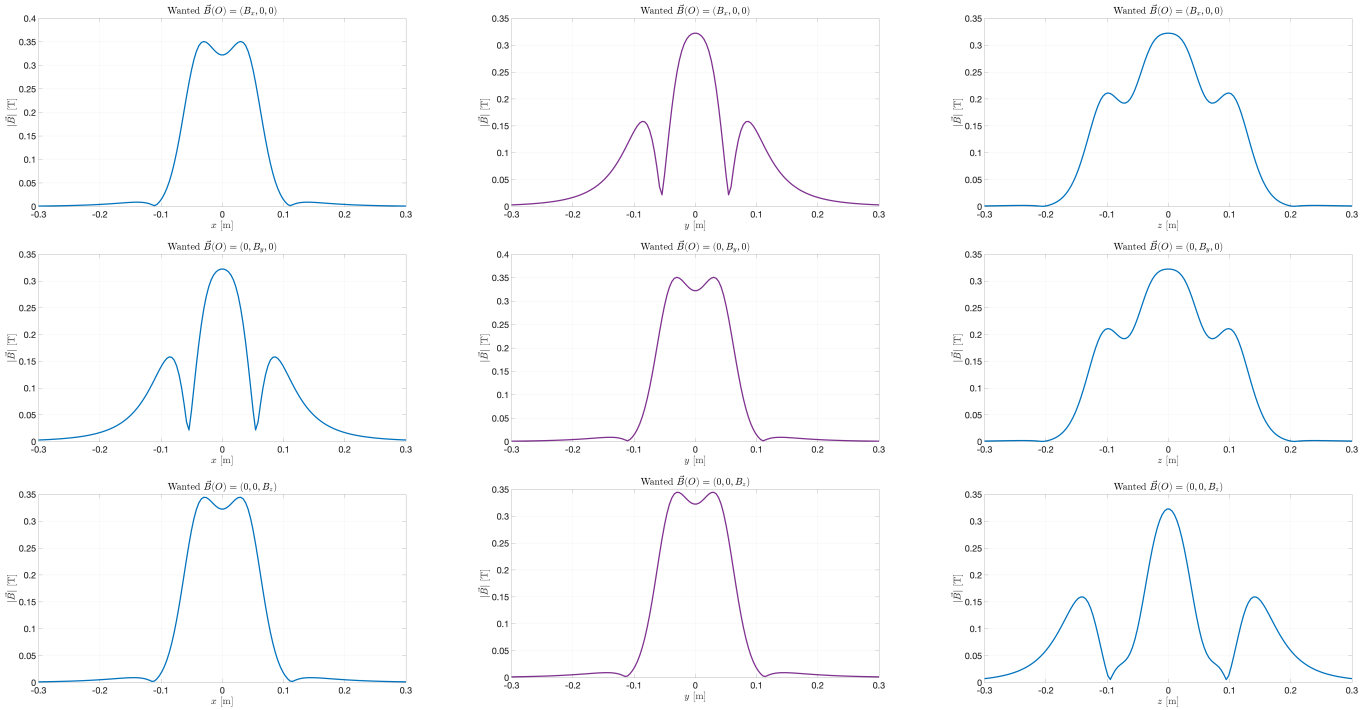

x y z

- No zero crossing of magnetic field along vertical jet (y) axis
- $B_y^{\min} \approx 1.9\,\mathrm{mT}$ sufficient to avoid **Majorana depolarization**
- Field integrals along beam (z) axis

$\vec{B}(O)$	$\parallel \vec{e}_x$	$\parallel \vec{e}_y$	$\parallel \vec{e}_z$
$\int \lvert\vec{B}\rvert \mathrm{d}z$	0.0667 Tm	0.0667 Tm	0.0546 Tm

pC polarimetry, spare slides

More complete picture using asymmetric beams at EIC

RHIC, EIC injection and EIC flattop (derived from [1], see also slide 58)

Metric	RHIC	T_{max} [K]	EIC inj.	T_{max} [K]	EIC flattop	T_{max} [K]
Target length ℓ [mm])	**25**		**50**		**50**	
Number of bunches	120		290		1160	
Protons / bunch ($\times 10^{10}$)	20.0		27.6		6.9	
σ_x^{95} [mm]	0.56	2130	8.60	**52**	3.94	**869**
σ_y^{95} [mm]	0.56	2130	1.69	**600**	0.66	**2665**
Equiv. round σ_r^{95} [mm]	0.56	2130	3.81	144	1.61	1610
$4\sigma_x^{95}$ [mm]	2.24		34.4		15.8	
$4\sigma_y^{95}$ [mm]	2.24		6.76		2.64	
Coverage $\ell/(4\sigma_x^{95})$	11.2		**1.45**		3.16	
Coverage $\ell/(4\sigma_y^{95})$	11.2		7.40		18.9	

Comments

1. Equivalent round size for thermal modeling: $\sigma_r^{95} = \sqrt{\sigma_x^{95}\,\sigma_y^{95}}$.
2. Rotation of setup by $\approx 45^\circ$ about $\vec{e}_z \Rightarrow T < T_{sub}$ at EIC injection for y' scan.
3. Length of horizontal ribbon is limiting case at EIC injection.

Direct measurement of temperature of carbon targets

Work with Frank Rathmann, Prashanth Shanmuganathan, Oleg Eyser, Haixin Huang, Dannie Steskie, Thomas Tsang, and George Mahler

- Carbon fiber targets of RHIC polarimeters do not reach carbon sublimation temperature[a] of $T_{\text{sub}} = 3915\,\text{K}$ [12]:
  - **targets survive proton bombardment** at RHIC.
  - Observation aligns coarsely with energy loss calculations by Peter Thieberger (BNL) using appropriate beam sizes at the interaction point.
- Direct temperature measurement of carbon targets remains crucial goal
  - Black-body radiation [24] as a method to determine temperature by analyzing the emitted light spectrum.

[a] Ref. [23] gives sublimation temperatures at one atmosphere pressure of 3895 K to 4020 K.

Carbon sublimation (Hertz–Knudsen) I

Thermodynamics vs. operations

- At $\sim$1 atm, carbon has no melt; it **sublimes** near $T_{\mathrm{sub}} \approx 3915\,\mathrm{K}$ (graphite) [23].
- In high/ultra-high vacuum the **vapor pressure** $P_{\mathrm{vap}}(T)$ controls the mass loss; practical ceilings for longevity are typically $\lesssim 3200\,\mathrm{K}$ to $3500\,\mathrm{K}$ depending on geometry/surface condition and allowed erosion.
- Thin ribbons/films (large area, edge density) show higher evaporation rates at the same T than bulk graphite; coatings change emissivity and kinetics.

Carbon sublimation (Hertz–Knudsen) II

Hertz-Knudsen flux (vacuum evaporation/sublimation)

$$J = \alpha \frac{P_{\mathrm{vap}}(T) - P_{\mathrm{amb}}}{\sqrt{2\pi\, m\, k_{\mathrm{B}}\, T}}, \qquad \frac{\dot{m}}{A} = J\, m. \tag{24}$$

- J [$\mathrm{m^{-2}\,s^{-1}}$]: flux (particles per unit area per unit time).
- α [1]: evaporation/accommodation coefficient ($0 \le \alpha \le 1$).
- $P_{\mathrm{vap}}(T)$ [Pa]: equilibrium vapor pressure at surface temperature T.
- P_{amb} [Pa]: ambient partial pressure of the same vapor species.
- m [kg]: molecular mass of the evaporating species (e.g., C or C_2).
- k_{B} [$\mathrm{J\,K^{-1}}$]: Boltzmann constant.
- T [K]: absolute surface temperature.
- $\dot{m}/A$ [$\mathrm{kg\,m^{-2}\,s^{-1}}$]: mass loss rate per unit surface area .

Carbon sublimation (Hertz–Knudsen) III

When $P_{\text{amb}} \approx 0$ (high/ultra-high vacuum)

$$\frac{\dot{m}}{A} \approx \alpha \, \frac{m \, P_{\text{vap}}(T)}{\sqrt{2\pi \, m \, k_{\text{B}} \, T}} = \alpha \, \frac{\sqrt{m} \, P_{\text{vap}}(T)}{\sqrt{2\pi \, k_{\text{B}} \, T}} \, . \tag{25}$$

- For $P_{\text{vap}}(T)$ and usage in UHV, see [25–27].

Experimental setup

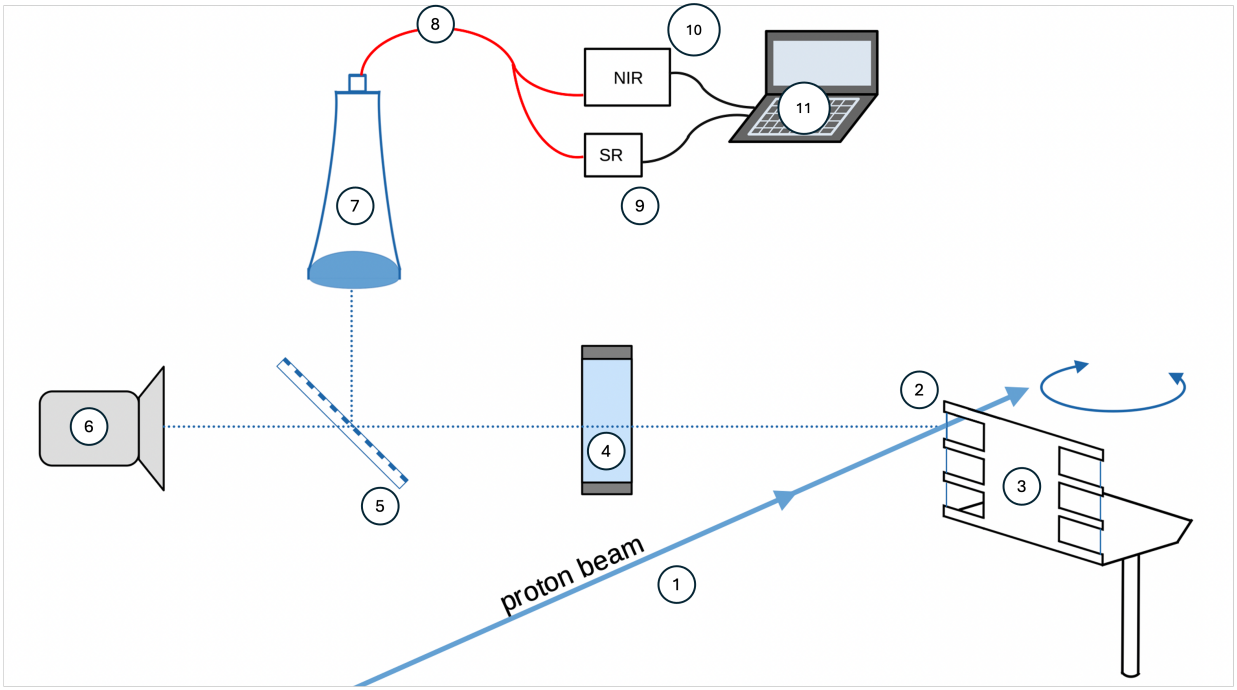

1. proton beam
2. fiber target
3. target holder
4. fused-silica viewport
5. semi-transparent polka-dot mirror
6. optical camera
7. collimator lens
8. fiber splitter (VIS and IR)
9. spectrometer VIS (SR)
10. spectrometer IR (NIR)
11. spectral analysis ($\lambda = 200 - 2200\,\text{nm}$)

Black body radiation

Ideally, one would measure:

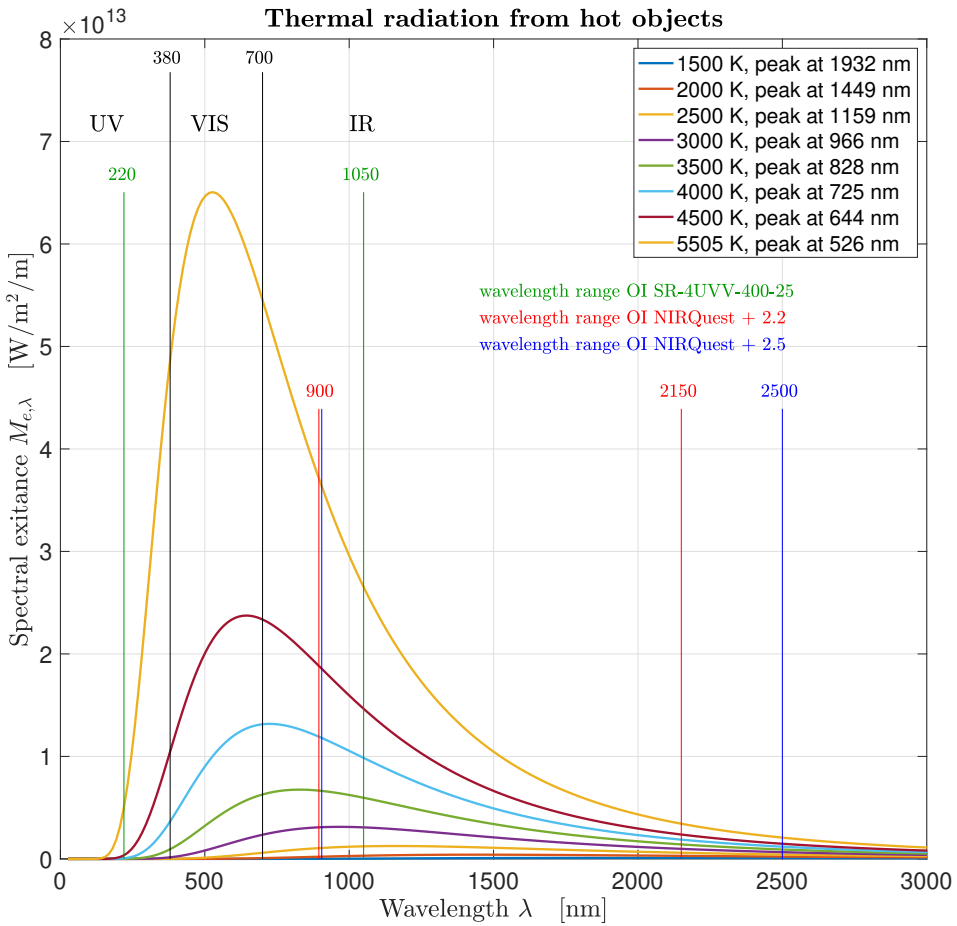

wavelength-dependent attenuation in

- fused-silica viewport
- collimator lens
- 100 m glass fibers from IP12 to spectrometers

Lab test measurement using IR light source

Experimental setup

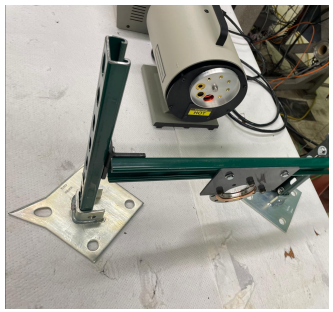

Black body radiation using oven at 1463 K

- SR spectrometer: 200 to 900 nm
- NIR spectrometer: 900 to 2100 nm
- Light path includes fiber splitter and 100 m glass fibers
- Measured spectrum compared to blackbody radiation spectra at 1463 K, 1263 K, and 1663 K

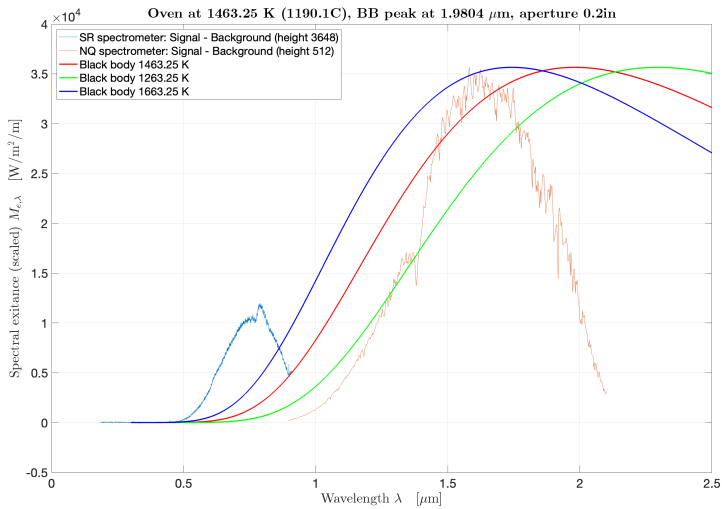

Test measurements using C targets at IP4

- In 2024, equipment/components arrived late, thus optimal alignment of light collection system at IP4 was not possible.
- We observe a clear signal, however, the light intensity is low because we don't aim at the brightest spot on the target
- For the same reason, the temperature we observe is only around 1400 K, about half of what we would expect

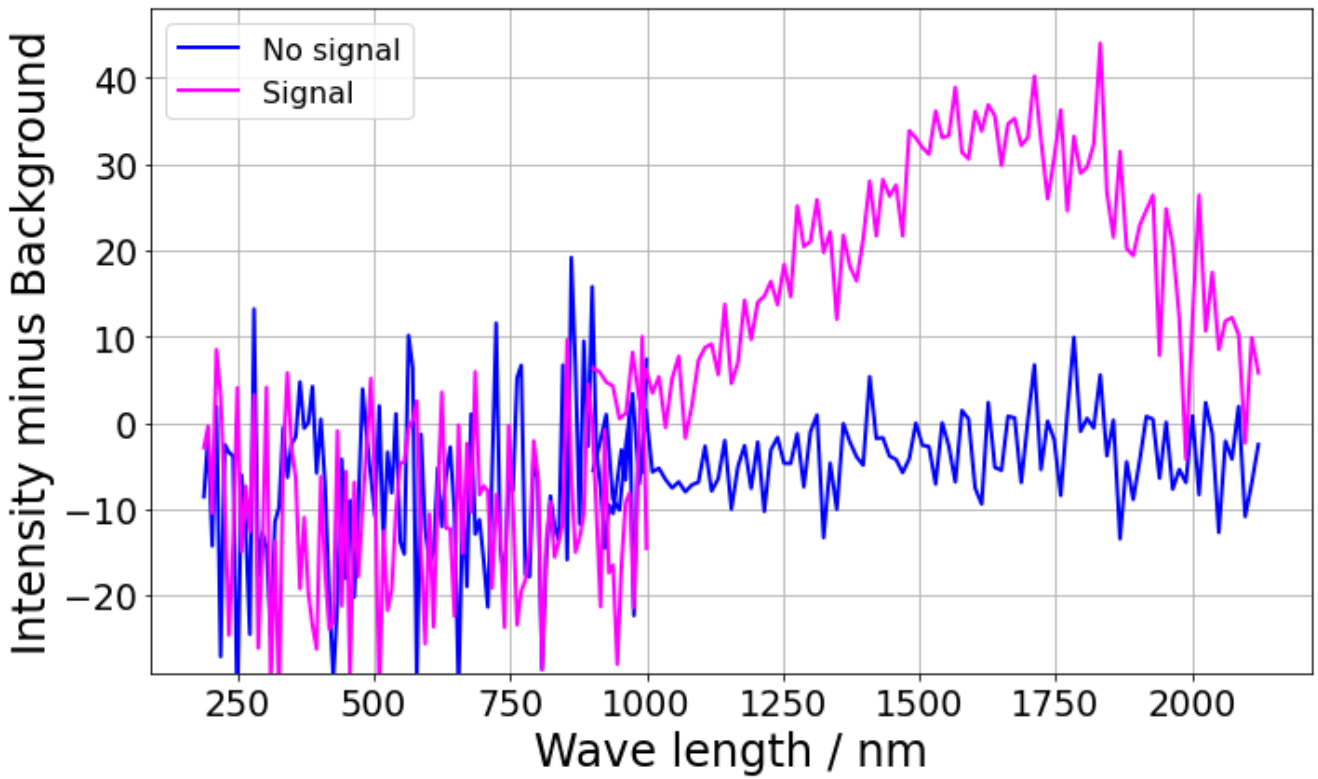

$\vec{d}$C Low Energy Polarimeter (LEP) used at COSY [28] I

Purpose

- LEP developed to measure **vector and tensor polarizations** of stored deuteron beams at injection energy (75.6 MeV) through elastic $\vec{d}$C scattering.
- Provides continuous monitoring of beam polarization during injection and acceleration cycles.

Experimental Setup

- Installed in the injection line of COSY, equipped with an ultra-high vacuum beam pipe and retractable thin carbon target.
- Four plastic scintillator detectors placed at azimuthal angles $\phi = 0°, 90°, 180°, 270°$ and polar angles $\theta \approx 25°$–$70°$.
- Detection geometry optimized for simultaneous sensitivity to vector (p_z) and tensor (p_{zz}) polarization components.

$\vec{d}$C Low Energy Polarimeter (LEP) used at COSY [28] II

Polarization Extraction

- Measured yield for elastic $\vec{d}\,C$ scattering:

$$N(\theta,\phi) = N_0(\theta)\left[1 + \tfrac{3}{2} p_z A_y(\theta)\cos\phi + \tfrac{1}{4} p_{zz} A_{yy}(\theta)(1+\cos 2\phi)\right] \tag{26}$$

  A_y and A_{yy} are vector and tensor analyzing powers

- **Vector polarization** from left–right asymmetry

$$p_z = \frac{2}{3A_y}\,\frac{N_L - N_R}{N_L + N_R} \tag{27}$$

- **Tensor polarization** from fourfold azimuthal pattern

$$A_T = \frac{(N_L + N_R) - (N_U + N_D)}{(N_L + N_R) + (N_U + N_D)}\,, \tag{28}$$

  where N_L, N_R, N_U, N_D are count rates in left ($\phi = 0°$), right (180°), up (90°), and down (270°) detectors. Tensor polarization follows

$$p_{zz} = \frac{4\,A_T}{A_{yy}\,(1 - A_T)}\,. \tag{29}$$

Analyzing powers and calibration, $\vec{d}C$ elastic scattering III

$\vec{d}C$ elastic data

- A_y at 75.6 MeV
  - S. Kato *et al.*, *Nucl. Instrum. Methods A* **238**, 453 (1985)
  - E. J. Stephenson, private comm. (76 MeV data)
- Combined value used in COSY experiments

$$A_y(40^\circ) = 0.61 \pm 0.04 \tag{30}$$

- Tensor analyzing powers A_{yy} negligible at this energy; LEP primarily measured p_z.
- A similar polarimeter needs to be designed to measure p_z, p_{zz} behind ion source at BNL.

^{3}He jet target thickness I

- **Given**
  - Flux $I = 1 \times 10^{14}\,\mathrm{s}^{-1}$, temperature $T = 1.3\,\mathrm{K}$, $m_{^3\mathrm{He}} \approx 3.016\,\mathrm{u}$.
  - Jet diameter $D = 1.0\,\mathrm{cm}$ (uniform profile) $\Rightarrow$ area $A = \pi(D/2)^2$.
  - Ion beam fully inside jet; line length along beam $L = 1\,\mathrm{cm}$.
  - Mean speed (Maxwell): $\bar{v} = \sqrt{\dfrac{8 k_\mathrm{B} T}{\pi m}}$.
  - Volume density [cm^{-3}]: $\rho = \dfrac{I}{\bar{v}\, A}$.
  - Areal density (target thickness): $d_t = \displaystyle\int \rho \,\mathrm{d}\ell \approx \rho L = \frac{I\, L}{\bar{v}\, A}$.
  - $\bar{v} \approx 9.6 \times 10^3\,\mathrm{cm\,s}^{-1}$ (for ^{3}He at 1.3 K).
  - $A = \pi(0.5)^2\ \mathrm{cm}^2 \approx 7.85 \times 10^{-1}\,\mathrm{cm}^2$.
- **Areal density of ^{3}He jet**

$$d_t = \rho\, L \approx 1.3 \times 10^{10}\ \mathrm{atoms\,cm}^{-2}. \tag{31}$$

  - *Scaling* $d_t \propto IL/(A\sqrt{T})$ with $A \propto D^2$.

^{3}He jet target thickness II

Storage cell (molecular–flow model [17]), cooled at $T = 77\,\mathrm{K}$

- **Geometry** (all $d = 1.0\,\mathrm{cm}$):
  - Injection tube: $\ell_{\mathrm{inj}} = 10\,\mathrm{cm}$.
  - Beam tubes: $\ell_{\mathrm{up}} = \ell_{\mathrm{down}} = 30\,\mathrm{cm}$.
  - Cell length along beam: $\ell_t = 60\,\mathrm{cm}$.
- **Molecular–flow tube conductance** [17, Eq. (13)]:

$$C_{\mathrm{tube}} \;=\; 3.81\,\sqrt{\frac{T}{M}}\;\frac{d^3}{\ell\left[\,1 + 1.33\,(d/\ell)\,\right]}. \tag{32}$$

  - C_{tube} in $\mathrm{L\,s^{-1}}$, d, ℓ in cm, T in K, M in $\mathrm{g\,mol^{-1}}$.
- **Total cell conductance** (for ^{3}He, $T = 77\,\mathrm{K}$):
  - Using the three–tube geometry above and $M = 3.016\,\mathrm{g/mol}$,

$$C_{\mathrm{tot}} \;\approx\; 2.92\,\mathrm{l/s} \;=\; 2.92 \times 10^3\,\mathrm{cm^3\,s^{-1}}.$$

^{3}He jet target thickness III

Thickness from cell balance (triangular $\rho(z)$ about center)

- **Steady state:** particle throughput equals outflow through total conductance, hence center volume density

$$\rho_0 = \frac{I}{C_{\text{tot}}} \tag{33}$$

- **Areal density along full cell length ℓ_t:**

$$d_t = \frac{1}{2}\,\rho_0\,\ell_t = \frac{1}{2}\,\frac{I\,\ell_t}{C_{\text{tot}}}. \tag{34}$$

- **Numerical result** (77 K, ^{3}He):

$$d_t \approx 1.0 \times 10^{12}\ \text{atoms}\,\text{cm}^{-2}. \tag{35}$$

- Result scales as $d_t \propto I\,\ell_t / C_{\text{tot}}$.

CNI recoil energies, angles, and cell wall thickness I

Recoil energy in the CNI region

- Recoil proton kinetic energy for elastic pp scattering on hydrogen target

$$T_R = \frac{|t|}{2m_p}, \tag{36}$$

the characteristic CNI range is $|t| \sim 10^{-4}$–10^{-2} GeV^2

- At high energy, the beam-scattering angle for the forward proton is

$$\theta_{\mathrm{lab}} \approx \frac{\sqrt{|t|}}{p_{\mathrm{lab}}}. \tag{37}$$

$\lvert t\rvert$ [GeV^2]	T_R [MeV]	θ_{lab} [mrad]	θ_{lab} [mrad]	θ_{lab} [mrad]	R_{PTFE} [μm]
E_{beam} [GeV]		3.0	23.5	250.0	
10^{-4}	0.053	3.51	0.43	0.04	0.88
10^{-3}	0.533	11.10	1.35	0.13	8.79
3×10^{-3}	1.60	19.22	2.33	0.22	26.4
10^{-2}	5.33	35.09	4.26	0.40	87.9

CNI recoil energies, angles, and cell wall thickness II

Teflon (PTFE) foil with $\rho = 2.2\,\mathrm{g\,cm^{-3}}$

- IUCF target cell used foil thickness of $d_t = 0.43\ \mathrm{mg/cm^2}$ [4] $\Rightarrow$ physical wall thickness $d_{\mathrm{wall}} = d_t/\rho \approx 2\,\mu\mathrm{m}$
- A $\approx 2\,\mu$m PTFE wall permits full transmission for $T_R \gtrsim 0.3$–0.4 MeV.
- Proton range given by stopping-power integral

$$R(E) = \int_0^E \mathrm{d}E' \,/(\mathrm{d}E'/\mathrm{d}x) \propto E^{1.7}\,, \tag{38}$$

  $\mathrm{d}E/\mathrm{d}x$ from standard compilations (e.g. SRIM, NIST PSTAR).
- Estimated proton range for PTFE foil in table obtained from linear scaling $R_{\mathrm{PTFE}}(T_R) \approx 16\,\mu\mathrm{m}\,(T_R/1\,\mathrm{MeV})$, anchored at 1 MeV range.

CNI recoil energies, angles, and cell wall thickness III

Multiple scattering in a 2 µm PTFE wall

- Multiple scattering mainly broadens the hit position on the silicon detector and does not significantly change the recoil energy T_R used for kinematic reconstruction.
- Highland approximation for the rms scattering angle

$$\theta_0 \simeq \frac{13.6\ \text{MeV}}{\beta pc} \sqrt{\frac{x}{X_0}}\,, \tag{39}$$

  where $x = 4.3 \times 10^{-4}\,\text{g}\,\text{cm}^{-2}$ is the areal thickness of a 2 µm PTFE wall and $X_0 \approx 34\,\text{g}\,\text{cm}^{-2}$ is the PTFE radiation length.
- For CNI recoil protons with $T_R \sim 0.3\,\text{MeV}$ to $1\,\text{MeV}$, θ_0 of order few mrad.
- Position smearing at the detector radius $r = 85\,\text{mm}$

$$\sigma_\perp = r\,\theta_0 \sim 0.2\,\text{mm to } 1\,\text{mm}. \tag{40}$$

CNI recoil energies, angles, and cell wall thickness IV

CNI compatibility of a 2 µm PTFE storage-cell wall

- Sufficient transmission for all CNI-relevant recoils ($T_R \gtrsim 0.3\,\mathrm{MeV}$).
- Multiple scattering: sub-millimeter position smearing at $r = 85\,\mathrm{mm}$.
- Compatible with CNI-based polarimetry at AGS energies (3 GeV to 23.5 GeV).